CENTRO DE INVESTIGACIONES
EN OPTICA, A.C.

“ANALYSIS OF SPIN-ORBIT COUPLING IN VECTOR BEAMS PROPAGATING THROUGH A DOVE PRISM”

<<Versión definitiva: Incluye cambios sugeridos por revisores>>

Tesis que para obtener el grado de Maestro en Ciencias (Óptica)

Presenta: Gabriela Flores Cova

Director de Tesis: Dr. Carmelo Rosales Guzmán

Vo. Bo.

León · Guanajuato · México
Junio de 2025

Acknowledgements

A la Secretaría de Ciencia, Humanidades, Tecnología e Innovación (SECIHTI), anteriormente conocida como CONAHCYT, por el respaldo económico otorgado mediante la beca que hizo posible la realización de mis estudios de maestría. Este apoyo fue esencial para poder dedicarme de tiempo completo a mi formación y a este proyecto de investigación. También agradezco al Centro de Investigaciones en Óptica (CIO) por brindarme el espacio, los recursos y el entorno académico necesarios para llevar a cabo este trabajo.

A mi director de tesis, el Dr. Carmelo Rosales Guzmán, a quien agradezco profundamente por su orientación, su paciencia y sus aportaciones a lo largo de este trabajo. Su acompañamiento fue clave para llegar hasta aquí.

A mis padres, Emilia y Martín, por su amor incondicional y por ser siempre mi mayor impulso. Su ejemplo de esfuerzo, coraje y amor por la ciencia ha sido una guía constante en mi vida.

A mis hermanos, Verónica y Luis Martín, por su apoyo inquebrantable y por acompañarme con cariño en cada paso de este recorrido. Su presencia ha sido un pilar fundamental en este proceso.

Y a todas las personas que estuvieron cerca durante esta etapa, dejando huellas significativas en mi formación académica y humana.

A Andrea.

Abstract

The strong coupling between spatial and polarization degrees of freedom in vectorial structured light beams gives rise to structured light fields with rich and versatile behavior. This intrinsic coupling has driven significant recent interest in their study and application across various fields.

This thesis primarily focuses on analyzing the interaction between a Dove prism and vortex vector beams. While the individual effects of a Dove prism on light polarization and orbital angular momentum (OAM) are well-documented, its influence on vector beams, where these degrees of freedom are fundamentally coupled, has remained largely unexplored. Our investigation reveals that the impact of Dove prisms on vector beams differs significantly from what might be anticipated by considering polarization or OAM independently. For instance, a polarization-only prediction might suggest a linear pattern transforming into a mix of linear and elliptical polarization. Similarly, an OAM-only perspective would merely anticipate a reversal of the OAM value and beam rotation.

However, our findings, supported by theoretical calculations, simulations, and experimental results, demonstrate a more complex behavior. To accurately model this phenomenon, we developed an extended Jones matrix that combined the effect of dove prisms on both the OAM and polarization degrees of freedom. A MATLAB code was created to simulate these effects, and the experimental results show excellent agreement with our theoretical models. A key result is that when polarization and OAM are coupled within a vector beam, the dove prism not only reverses the sign of the OAM but also induces an intermodal phase shift. This remarkable effect enables a smooth transition between fundamental vector beam types, specifically azimuthal and radial polarizations, as well as their hybrid states.

As an additional contribution, this work also introduces two novel forms of vector beams: Vector Vortex Pearcey-Gauss beams and curvilinear polarized beams, which were constructed for the first time. These beams were named on the basis of the distinctive shape of their electric field distributions, which exhibit characteristic curvilinear and vortex-like polarization patterns, and in the case of the Vector Vortex Pearcey-Gauss

beams are distinguished by an intensity profile that resembles a caustic-shaped pattern, characteristic of the Pearcey function. The insights gained from this research significantly advance our understanding of vector beam manipulation and lay the groundwork for their advanced applications in various optical systems.

Contents

List of Figures

1 | Introduction

Light, as an electromagnetic wave, has numerous degrees of freedom (DoFs), including phase, amplitude, polarization, frequency, and angular momentum. All of this fully defines the state of an optical field and they can be manipulated by specific optical components, facilitating the creation of beams with tailored characteristics. This meticulous control of its DoFs has enabled innovative applications across various scientific and technical fields, including high-resolution microscopy, image processing algorithms, optical communication systems, and optical trapping techniques, among others. The DoFs can be adjusted either independently or in a coupled manner, resulting in the formation of vector beams. Such beams are characterized by their spatially varying and complex polarization distributions. They have been studied in depth in recent years due to their inherent flexibility and unique properties.

This thesis analyzes the interaction between vectorial light fields, coupled in spin and orbital angular momentum, and a Dove prism (DP). The prism's influence on independent polarization and orbital angular momentum (OAM) is well established. Nonetheless, the case in which these DoFs are coupled, a fundamental feature of vector beams, remains mostly unexamined. Comprehending the prism's impact on these interconnected features is crucial for using vector beams in optical systems.

The thesis is organized as follows. First, in Chapter 2, we establish the theoretical basis for the subsequent chapters. This chapter covers the fundamentals of structured light and is divided into four sections. The first section explains what scalar beams are, how they arise from solving the wave equation in different coordinate systems, and presents examples of various beam families. The second section introduces the concept of vector beams, emphasizing the differences between them and scalar beams. The third section discusses methods for generating these types of beams, focusing on two main techniques: using q-plates and spatial light modulators (SLMs). Finally, the fourth section explores Stokes polarimetry, a crucial tool for analyzing the polarization patterns of vector beams. Chapter 3 focuses on the generation of two novel types of vector beams and is divided into two sections. The first discusses Pearcey-Gauss beams, while the second explores curvilinear polarized beams. Chapter 4 discusses

the analysis of the effect of a DP on vector beams. This chapter is divided into six sections, beginning with an examination of how a rotating DP influences scalar beams, with particular attention to polarization (Section 4.1). Section 4.2 continues the study of scalar beams by analyzing the effect of the prism on the OAM of light. Section 4.3 extends the Jones matrix formalism to describe the interaction of vector beams with the DP, offering a generalized framework that accounts for both the spatial and polarization DoFs. In Section 4.4, a numerical simulation is presented to model the theoretical predictions, followed by a description of the experimental setup used to validate these results in Section 4.5. Finally, Section 4.6 presents and discusses the experimental results, highlighting the key findings and comparing them with the theoretical and simulated expectations.

2 | Structured beams

At a certain stage in optics research, the use of conventional laser modes proved to be insufficient for specific applications [1]. This limitation gave rise to the field of structured light, which focuses on exploring field distributions with novel characteristics and developing techniques to shape light accordingly. These tailored field distributions are achieved by controlling the DoFs of light—that is, its amplitude, polarization, and phase—typically using SLMs [2]. The ability to tailor light in such precise ways has transformed both fundamental research and practical technologies, paving the way for innovations in fields such as optical trapping and tweezing [3], quantum information processing [4], mode division multiplexing [5], advanced microscopy [6], 3D holographic imaging and metrology [7, 8, 9], and even laser design [10, 11].

This chapter first introduces the fundamental properties of scalar beams, focusing on two widely used modes that arise from solving the wave equation in different coordinate systems: Laguerre and Hermite-Gauss beams. The discussion then change to vector beams, highlighting their unique polarization structures and the methods used for their generation, including numerical simulations and experimental techniques that involve optical elements such as q-plates and SLMs. Finally, we will address the characterization of structured light using Stokes polarimetry.

2.1 Scalar beams

The simplest approach to structuring light involves shaping its field distribution by controlling its phase and amplitude, while leaving polarization as a free degree of freedom (DoF) in the design process. The former leads to various spatial modes, which are specific solutions to the Helmholtz equation in its exact form [12]:

$$\nabla^2 E(\mathbf{r}) = -E(\mathbf{r})k^2, \tag{2.1}$$

where $E(\mathbf{r})$ is the electric field as a function of the position vector $\mathbf{r} = (x, y, z)$, ∇^2 is the Laplacian operator, and $k = 2\pi/\lambda$ is the wavenumber, with λ being the wavelength of

the light in the medium.

In the paraxial approximation—valid when the field varies slowly along the propagation direction z—the Helmholtz equation reduces to the paraxial wave equation [13]:

$$\nabla_T^2 E_0(\mathbf{r}) - 2\mathrm{i}k\frac{\partial E_0(\mathbf{r})}{\partial z} = 0, \tag{2.2}$$

where $\nabla_T^2 = \frac{\partial^2}{\partial x^2} + \frac{\partial^2}{\partial y^2}$ is the transverse Laplacian operator, and $\partial/\partial z$ denotes the partial derivative with respect to the propagation direction.

These spatial modes can be grouped into distinct families based on the coordinate system chosen for solving the Helmholtz equation and its paraxial approximation. Typical examples of such vector modes include Bessel [14, 15] and Laguerre -Gauss [16] beams, for polar symmetry; Mathieu [17, 18] and Ince-Gauss beams [19], for elliptical symmetry; and more recently, parabolic [20, 21], helico-conical [22], and Pearcey [23] beams. We will now briefly discuss two of the most popular modes, the Laguerre-Gauss (LG) and the Hermite-Gauss (HG) beams.

2.1.1 Hermite-Gauss modes

If we solve the paraxial Helmholtz equation in a rectangular coordinate system, the solution can be expressed in the following form [24]:

$$HG_{u,n}(\mathbf{r}) = \psi_0 \left[\frac{\omega_0}{\omega(z)}\right] H_u\left(\frac{\sqrt{2}x}{\omega(z)}\right) H_n\left(\frac{\sqrt{2}y}{\omega(z)}\right) \dots \tag{2.3}$$

$$\dots \exp\left[i\left(-kz - \frac{k\rho^2}{2R(z)} + (u+n+1)\zeta(z)\right)\right],$$

where

$$H_p\left[\frac{\sqrt{2}q_i}{\omega(z)}\right] = \mathcal{H}_p\left(\frac{\sqrt{2}q_i}{\omega(z)}\right)\exp\left(-\frac{2q_i^2}{\omega^2(z)}\right), \quad \text{with } q_i = x, y, \tag{2.4}$$

is referred to as the HG function of order p, where $\mathcal{H}_p$ represents the Hermite polynomials. In this expression, ψ_0 denotes the initial amplitude of the beam, and ω_0 is the waist of the beam (the minimum radius of the beam) in $z = 0$. The parameter $\omega(z)$ describes the beam width as a function of z, while k is the wave number. The term $\rho^2 = x^2 + y^2$ represents the squared radial coordinate in the transverse plane. The function $R(z)$ corresponds to the radius of curvature of the beam's wavefronts, and $\zeta(z)$ is the Gouy phase, which introduces a phase shift that depends on z.

A beam with a complex amplitude described by Equation 2.3 is known as a Hermite-Gaussian mode of order (u, n), where u and n represent the number of nodes (null

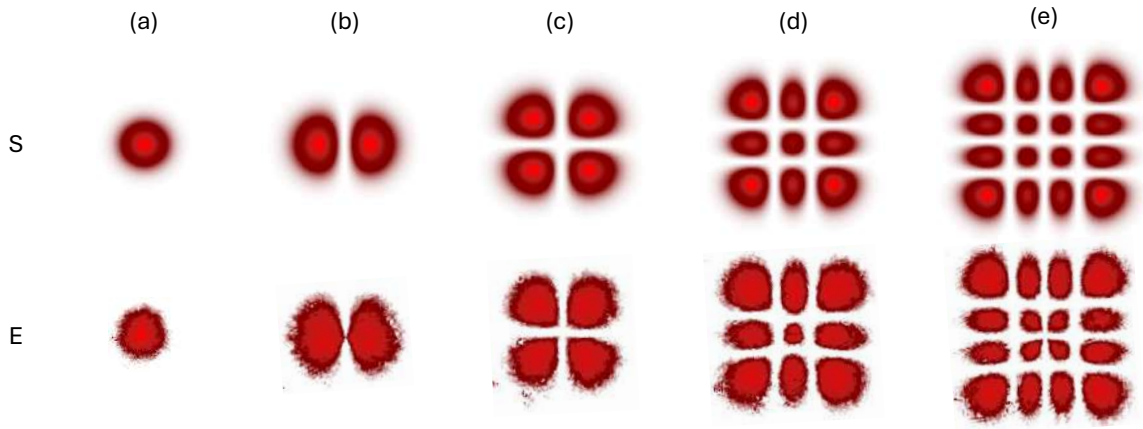

Figure 2.1: Intensity distribution for several HG beams in the transverse plane. Each column corresponds to a specific mode: (a) HG_{00}, (b) HG_{10}, (c) HG_{11}, (d) HG_{22}, and (e) HG_{33} . Numerical simulations (S) are on top and experiments (E) are on the bottom.

intensity points) along the x- and y-axes, respectively. The HG beam of order $(0, 0)$ corresponds to the fundamental Gaussian beam.

The intensity distribution of a $\mathrm{HG}_{u,n}$ is given by $I_{u,n} = |\mathrm{HG}_{u,n}|^2$, and it can be expressed as:

$$I_{u,n} = |\psi_0|^2 \left[\frac{\omega_0}{\omega(z)}\right]^2 H_u^2\left(\frac{\sqrt{2}x}{\omega(z)}\right) H_n^2\left(\frac{\sqrt{2}y}{\omega(z)}\right). \tag{2.5}$$

Figure 2.1 illustrates the experimental and simulated intensity distributions for Hermite-Gaussian beams in the transverse plane. It can be observed that higher-order beams (Figure 2.1e) exhibit broader spatial distributions compared to lower-order beams (Figure 2.1b). Additionally, the fundamental Gaussian beam (Figure 2.1a) is the only circularly symmetric member of the HG family.

Finally, it is important to highlight that the HG family forms a complete orthogonal basis, allowing any arbitrary beam to be represented as a superposition of Hermite-Gaussian modes [25].

2.1.2 Laguerre-Gauss modes

An alternative complete set of solutions, known as LG beams, is obtained by solving the paraxial Helmholtz equation in cylindrical coordinates (ρ, φ, z). The complex amplitude of the LG beam, denoted $LG_{\ell p}$, can be expressed as [2]

$$LG_p^{\ell}(\rho, \varphi, z) = \frac{\omega_0}{\omega(z)}\sqrt{\frac{2p!}{\pi(|\ell| + p)!}}\left(\frac{\sqrt{2}\rho}{\omega(z)}\right)^{|\ell|} L_p^{|\ell|}\left[2\left(\frac{\rho}{\omega(z)}\right)^2\right]\exp[-ikz] \tag{2.6}$$

$$\times \exp\left[i(2p+|\ell|+1)\zeta(z)\right] \exp\left[-\left(\frac{\rho}{\omega(z)}\right)^2\right] \exp\left[-\frac{ik\rho^2}{2R(z)}\right] \exp[-i\ell\varphi],$$

where

$$L_p^\ell(x) = \frac{x^{-\ell}e^x}{p!}\left(\frac{d^p}{dx^p}\right)\left[x^{\ell+p}e^{-x}\right], \tag{2.7}$$

are the generalized Laguerre polynomials. The parameters $\omega(z)$, $R(z)$, and $\zeta(z)$ are the same as those in HG beams. The integers $\ell = 0, 1, 2, \ldots$ (azimuthal index) and $p = 0, 1, 2, \ldots$ (radial index) represent the beam's mode structure. The lowest-order LG beam, LG_{00}, like the lowest-order HG beam, HG_{00}, is equivalent to the fundamental Gaussian beam.

The intensity $I_{\ell,p} = |LG_{\ell p}|^2$ of the LG modes is given by:

$$I_{\ell,p} = |\psi_0|^2 \left|\frac{\omega_0}{\omega(z)}\right|^2 \left[\frac{\sqrt{2}\rho}{\omega(z)}\right]^{2|\ell|} \left|L_p^{|\ell|}\left[\frac{2\rho^2}{\omega^2(z)}\right]\right|^2 \exp\left[-\frac{2\rho^2}{\omega^2(z)}\right],$$

and is a function of ρ and z but not of φ, meaning that the intensity is circularly symmetric (see Figure 2.2). Figure 2.2 illustrates various LG beam modes, including their simulated intensity distributions (top row) and experimentally generated counterparts (bottom row). The modes are labeled (a) through (e) and correspond to a fixed azimuthal index $\ell = 3$ and increasing radial indices $p = 0$ to $p = 4$. These images highlight the characteristic ring-like intensity profiles of LG modes, where the number of rings increases with the radial index p, while maintaining the same topological charge $\ell = 3$. These beams are also commonly referred to as optical vortices, a term that highlights

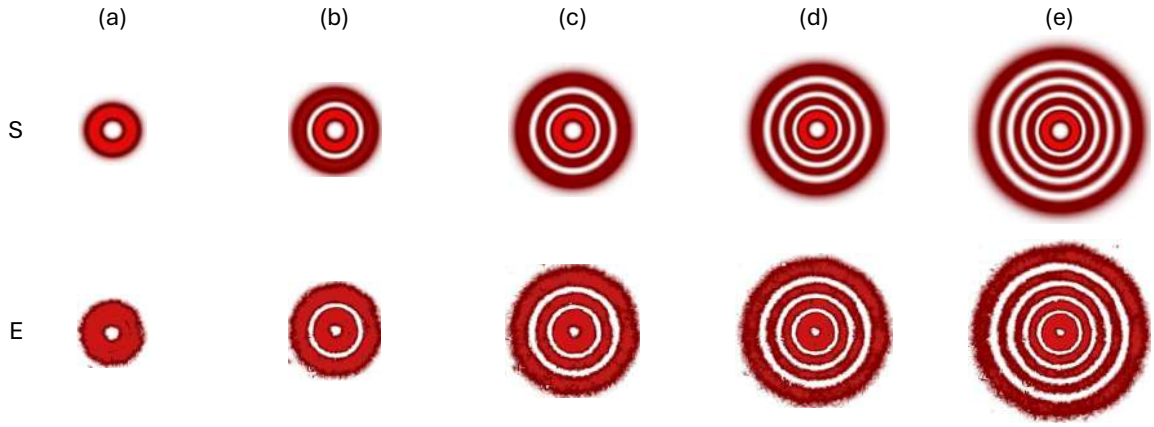

Figure 2.2: Simulated (S) and experimental (E) intensity profiles of LG modes. Each column corresponds to a fixed azimuthal index $\ell = 3$ and increasing radial indices p. The values of p are: (a) $p = 0$, (b) $p = 1$, (c) $p = 2$, (d) $p = 3$, and (e) $p = 4$.

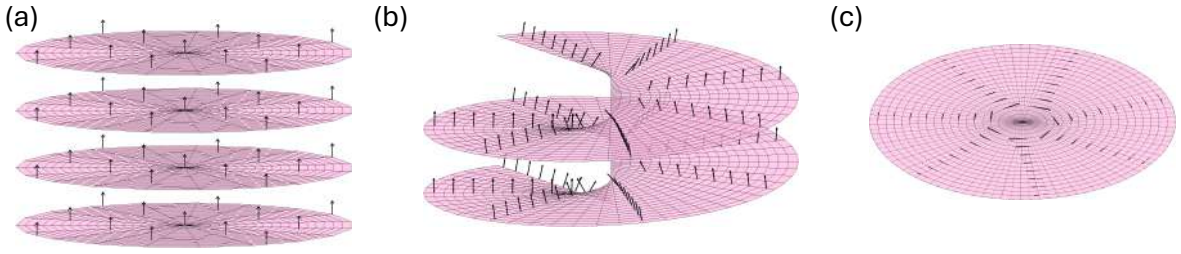

Figure 2.3: Wave-fronts of the electric fields; the plane wave (a) has linear momentum and the helical wave (b) has both linear and angular momentum. The Poynting vector of the beam is perpendicular to the wave but since the wave is twisted the Poynting vector is not in the direction of propagation anymore (c).

the phase singularity at the beam center. This singularity leads to a zero-intensity point at the center.

The phase behavior of the LG beam has the same dependence on ρ and z as the Gaussian beam, with two notable differences: (1) the Gouy phase is enhanced by the factor $(\ell + 2p + 1)$, and (2) there is an additional phase factor $e^{\pm j\ell\varphi}$ proportional to the azimuthal angle φ. This phase component, $\ell\varphi$, results in the wavefront taking the form of a helical structure as the beam propagates along z. For $\ell > 1$, the beam consists of ℓ intertwined helices, where the pitch of each helix is $\ell\lambda$, and the $\pm$ sign determines the handedness of the helices [24]. The helical wavefront structure of these beams directly gives rise to the presence of OAM; as the linear momentum of the optical wave, orthogonal to its wavefront, gains azimuthal components that revolve about the beam axis, as illustrated in Figure 2.3. Each photon in an LG beam with azimuthal index ℓ carries an OAM of $\ell\hbar$, where $\hbar$ is the reduced Planck constant. This property makes LG beams highly significant in applications such as quantum communication and microscopy [26, 27].

2.2 Generalities about vector beams

Another approach to structuring light involves manipulating various degrees of freedom simultaneously, such as, phase, amplitude, and polarization of a beam. An example of this and of interest for this thesis are vector beams, non separable in their spatial and polarization DoF, which are commonly generated as a non-separable weighted superposition of the form

$$U(\mathbf{r}) = \cos\Theta\, u_R(\mathbf{r})\, \hat{e}_R + \sin\Theta\, u_L(\mathbf{r})\, e^{i\delta}\, \hat{e}_L, \tag{2.8}$$

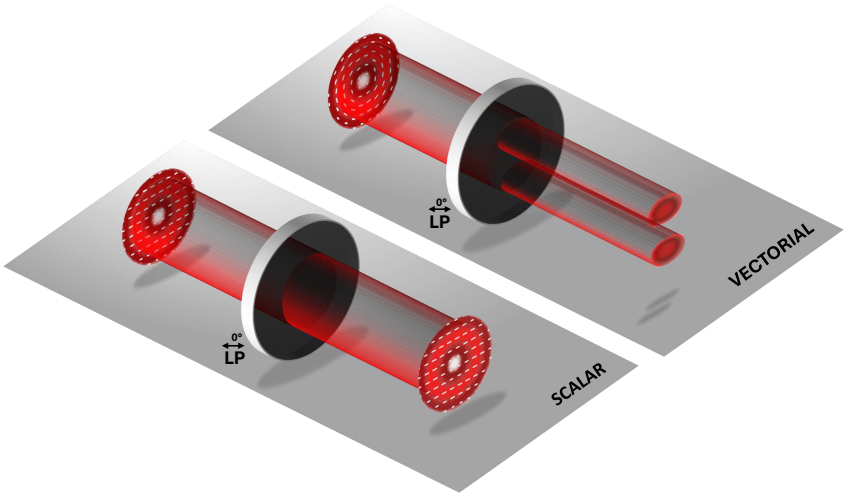

Figure 2.4: Scalar and vector beams: scalar beams have homogeneous polarization, whereas vector beams exhibit inhomogeneous polarization. As a consequence, when a scalar beam passes through a horizontal polarizer, its spatial mode remains unchanged apart from an overall amplitude reduction. In contrast, for a vector beam, passing through a horizontal polarizer modifies the spatial intensity distribution, revealing different patterns depending on the beam's polarization structure.

where $u_R(\mathbf{r})$ and $u_L(\mathbf{r})$ are orthogonal functions associated with the spatial DoF, and Θ is a weighting coefficient. The orthogonal unit vectors $\hat{e}_R$ and $\hat{e}_L$ represent right- and left-handed circular polarization states, respectively, while δ is the intermodal phase between the elements of the superposition [28, 2].

The non-separability of this superposition establishes a coupling between the DoFs of the beam, and also a pattern of inhomogeneous polarization. As a result, altering one DoFs, such as the spatial structure, inherently affects the other, such as the polarization state. In contrast with scalar beams that exhibit a uniform polarization that is independent of their spatial structure; hence, modifying their polarization does not alter their spatial form. This fundamental difference between scalar and vector beams, particularly the coupling between the DoFs, can be observed in Figure 2.4.

2.3 Generation of vector beams

As mentioned earlier, Equation 2.8 indicates that generating a vector beam requires the superposition of two orthogonal beams, both orthogonal in their spatial structure and polarization (see Figure 2.5). Such non-separable superposition can be simulated through numerical simulations using MATLAB. Using for example optical vortices we can generate cylindrical vector beams by giving equal weight to both components, i.e.,

setting $\Theta = \frac{\pi}{4}$, and choosing the spatial modes $u_R(\mathbf{r})$ and $u_L(\mathbf{r})$ as vortices with topological charges $\ell = \pm 1$, we can generate different vector beams. Furthermore, the intermodal phase δ can take values of 0 or π, leading to distinct polarization structures. These configurations result in four fundamental vector beams, described by the following equations [29]

$$U_R(\mathbf{r}) = u_R^{\ell=1}\,\hat{e}_R + u_L^{\ell=-1}\,\hat{e}_L, \tag{2.9}$$

$$U_A(\mathbf{r}) = u_R^{\ell=1}\,\hat{e}_R - u_L^{\ell=-1}\,\hat{e}_L, \tag{2.10}$$

$$U_{HR}(\mathbf{r}) = u_R^{\ell=-1}\,\hat{e}_R + u_L^{\ell=1}\,\hat{e}_L, \tag{2.11}$$

$$U_{HA}(\mathbf{r}) = u_R^{\ell=-1}\,\hat{e}_R - u_L^{\ell=1}\,\hat{e}_L. \tag{2.12}$$

These four modes are illustrated in Figure 2.6; the beam shown in (a) is known as radial mode, (b) is an azimuthal mode, (c) is a radial-hybrid mode, and (d) is an azimuthal-hybrid mode.

Experimentally, the most straightforward method to implement a wavefront reshaping, and thus generate these beams, is by introducing optics that make the optical path-length of the light beam vary across the beam transverse section, hence adding to the beam a spatially variant phase shift. This is achieved, for instance, by using a spiral phase plate or a SLM, both of which will be discussed in the following sections.

2.3.1 Experimental generation through q-plates

A q-plate is an optical element that can be fabricated using liquid crystals [30] or dielectric metasurfaces [31]. In its LC-based form, a q-plate consists of an azimuthal arrangement of the molecular director around a central singularity. This pattern is primarily characterized by the topological charge q, which can take integer or half-integer values. In particular, a q-plate with $q = 1$ exhibits global rotational symmetry around its

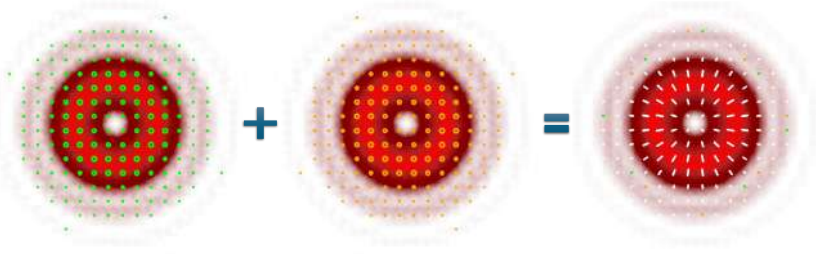

Figure 2.5: Superposition of two orthogonal modes with orthogonal polarization states. The orange and green circles within each mode represent right- and left-handed circular polarization respectively, while the white radial lines in the resulting mode indicate linear polarization.

center and enables a direct conversion of SAM into OAM within the same beam, without any net angular momentum exchange with the medium. This phenomenon is known as spin-to-orbital angular momentum conversion [32]. More generally, q-plates with arbitrary topological charges q allow the generation of light beams carrying an OAM of $2q\hbar$ per photon, with the OAM sign determined by the input polarization.

When a q-plate is illuminated with a uniformly polarized beam, it imposes a space-dependent phase, converting the input polarization into a spatially varying distribution. For an incident circularly polarized beam, the q-plate flips the polarization handedness and imparts an azimuthal phase factor $e^{\pm 2iq\varphi}$, generating an optical vortex. If the input beam is linearly polarized, it can be expressed as a superposition of left- and right-handed circular polarization components:

$$\mathbf{E}_{\text{LP}} = \frac{1}{\sqrt{2}} \left(\mathbf{E}_{\text{LCP}} + \mathbf{E}_{\text{RCP}} \right), \tag{2.13}$$

where $\mathbf{E}_{\text{LCP}}$ and $\mathbf{E}_{\text{RCP}}$ represent the left- and right-circular polarization states, respectively. Upon passing through the q-plate, each circular component experiences a distinct transformation: the handedness of polarization is flipped, and an azimuthal phase factor $e^{\pm 2iq\phi}$ is introduced, where the sign depends on the initial handedness of the component. After propagation through the q-plate, the transformed components recombine, giving rise to a vector beam:

$$\mathbf{E}_{\text{out}} = \frac{1}{\sqrt{2}} \left(e^{+2iq\varphi} \mathbf{E}_{\text{RCP}} + e^{-2iq\varphi} \mathbf{E}_{\text{LCP}} \right). \tag{2.14}$$

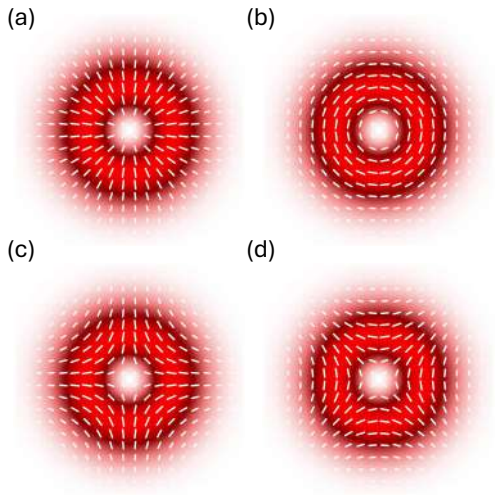

Figure 2.6: Polarization distributions of vector vortex beams with different polarization distributions. The white arrows represent the local polarization direction. (a) Radial polarization, (b) Azimuthal polarization, (c) and (d) Hybrid vector beams.

This results in a polarization state that varies across the transverse plane. For example, if the input linear polarization is horizontal, the output will be a radial polarization pattern, and if the input is vertical, the output will have azimuthal polarization, as illustrated in Figure 2.7 [33].

2.3.2 Experimental generation through spatial ligth modulators

A SLM is a device that modulates the phase of incident light, typically for a specific polarization—commonly horizontal. Although it does not directly modulate amplitude or polarization, complex amplitude modulation techniques can be employed to encode both amplitude and phase information into the phase pattern displayed on the SLM [34]. The operation of SLMs relies on the properties of LCs and can be implemented in either reflective or transmissive configurations. Fundamentally, an SLM consists of a pixelated display containing millions of individually controllable LC-filled cells.

One of the main advantages of SLM technology is its user-friendliness, as it does not require specialized software. Instead, it can be connected to a computer and utilized as an external monitor. By displaying grayscale images, the intensity of each pixel dictates the orientation of the LCs, enabling the modulation of an incident light beam [2].

Vector beams can be produced using the Sagnac-based optical arrangement shown

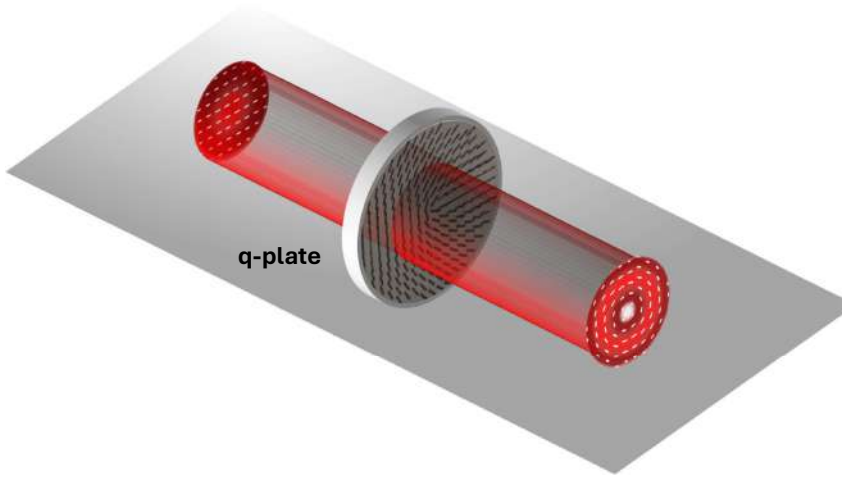

Figure 2.7: Schematic representation of a q-plate converting a scalar beam into a vectorial beam. The q-plate modifies the wavefront of the transmitted light, imprinting a helical phase structure.

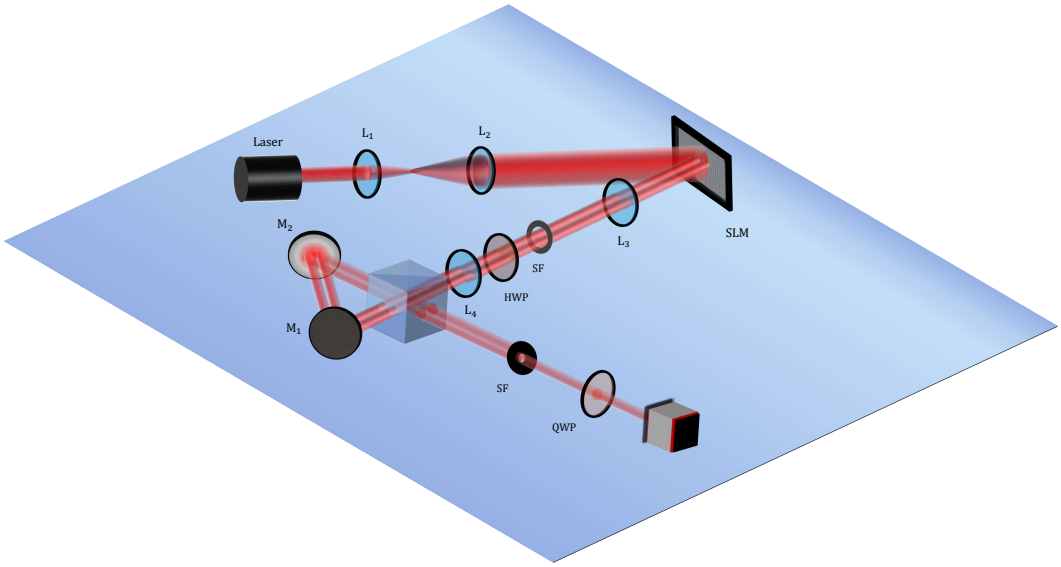

Figure 2.8: Schematic representation of a Sagnac-based experimental setup to generate vector beams using an SLM. PBS, polarizing beam splitter; M, mirror; HWP, half wave-plate; QWP, quarter wave-plate; L, lenses; SF, spatial filter.

in Figure 2.8 [35]. Initially, an expanded and collimated laser beam with horizontal polarization is directed toward two distinct regions of an SLM's screen, each programmed with an independent digital hologram. These holograms are specifically designed to generate the desired beam and incorporate a linear grating to separate and filter the first diffraction order of each hologram. The optical beams emerging from the SLM are subsequently passed through a half-wave plate oriented at 22.5 degrees to rotate their polarization state to diagonal. These beams then enter a common-path triangular Sagnac interferometer, whose principal component is a polarizing beam splitter (PBS). The PBS separates each beam into horizontal and vertical polarization components, which propagate along opposite directions within the interferometer. After completing a round trip, the interferometer outputs four beams—two with horizontal polarization and two with vertical polarization—on the opposite side of the PBS. To generate a vector beam, one beam from the first SLM region, carrying horizontal polarization, is overlapped with the corresponding beam from the second region, which has vertical polarization. The precise alignment required for this superposition can be digitally adjusted through the linear gratings encoded on the SLM. Additionally, a quarter-wave plate is introduced to convert the vector beam from a linear to a circular polarization state.

2.4 Polarization reconstruction: Stokes polarimetry

The transverse polarization distribution of a vector beam can be reconstructed using Stokes polarimetry, an intensity-based technique that determines the state of polarization. While conventionally requiring six intensity measurements for different polarization projections, it is possible to fully characterize the polarization state with only four [36].

The Stokes parameters are originally computed as [37]:

$$\begin{aligned} S_0 &= I_H + I_V, \\ S_1 &= I_H - I_V, \\ S_2 &= I_D - I_A, \\ S_3 &= I_R - I_L, \end{aligned} \tag{2.15}$$

where $I_H, I_V, I_D, I_A, I_R,$ and I_L are the intensities for horizontal, vertical, diagonal, anti-diagonal, right-circular, and left-circular polarizations, respectively. Since $S_0 = I_H + I_V$, we express $I_V = S_0 - I_H$ and substitute it into S_1:

$$S_1 = 2I_H - S_0. \tag{2.16}$$

Similarly, using $S_0 = I_D + I_A$, we obtain:

$$S_2 = 2I_D - S_0. \tag{2.17}$$

Since S_3 remains unchanged, the Stokes parameters can be determined with only four intensity measurements:

$$\begin{aligned} S_0 &= I_R + I_L, \\ S_1 &= 2I_H - S_0, \\ S_2 &= 2I_D - S_0, \\ S_3 &= I_R - I_L. \end{aligned} \tag{2.18}$$

Experimentally, I_R and I_L are acquired by passing the beam through the combination of a QWP and a LP. To measure the former, the QWP is set to an angle of $45°$, while the LP is set to $0°$; to measure the latter, the LP is rotated to $90°$. Finally, I_H and I_D are obtained by passing the beam through a LP oriented at $0°$ and $45°$, respectively. By way of example, Fig. 2.9(b) shows a set of experimentally measured intensity distributions, from which the Stokes parameters shown in Fig. 2.9(c) were computed. The corresponding transverse polarization pattern, reconstructed from these parameters, is presented in Fig. 2.9(a). The reconstruction of the polarization pattern is performed

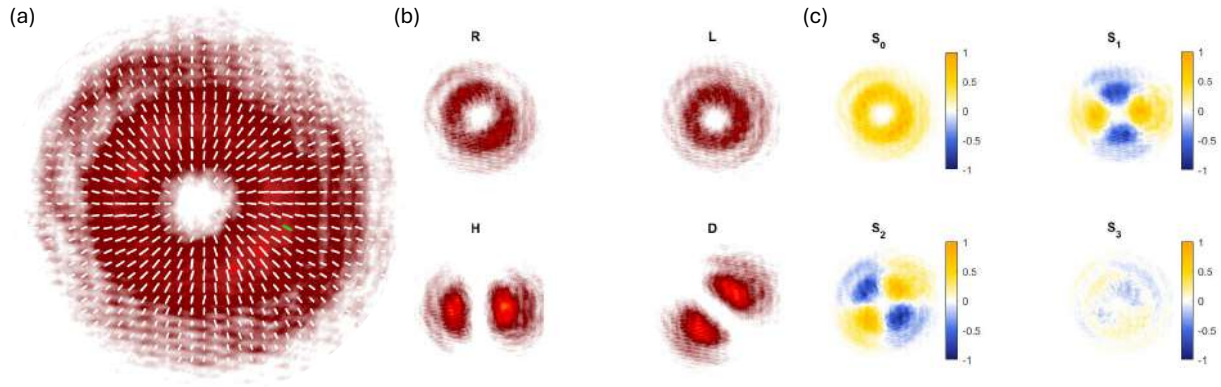

Figure 2.9: (a) Reconstructed transverse polarization pattern of a vector beam. (b) Experimentally measured intensity distributions for right-circular (*R*), left-circular (*L*), horizontal (*H*), and diagonal (*D*) polarization components. (c) Corresponding Stokes parameters S_0, S_1, S_2, S_3 obtained from these intensity measurements.

by dividing the transverse plane of the beam into small spatial regions and calculating the local Stokes parameters S_0, S_1, S_2, S_3 at each point. These parameters fully characterize the state of polarization at each position within the beam profile. From this information, the orientation and ellipticity of the polarization ellipse at every point can be retrieved, allowing visualization of the complete polarization distribution across the beam.

3 | Generation of new vector beams

The use of a SLM enables the generation of a wide variety of both scalar and vector beams due to its remarkable versatility. In the previous chapter, an experimental setup based on a Sagnac interferometer was briefly described for the generation of vector beams. However, such beams can also be produced without relying on an interferometric configuration.

This chapter presents two alternative techniques for generating vector beams, both developed as part of research studies in which I participated. One of these studies has already been published, while the other is currently in the writing process. The experimental methodology and results will be detailed, highlighting the first-time generation of two distinct types of vector beams.

3.1 Scalar and Vector Vortex Pearcey-Gauss Beam Generation

Light can naturally form intricate structures that may seem almost unreal, yet they emerge purely from its interaction with the environment. A striking example of such phenomena is the formation of caustics, which can be observed in everyday scenarios such as the patterns at the bottom of swimming pools, within a cup of coffee, or in the shadow of a glass when light strikes it at a certain angle. These structures arise from the concentration of light rays along curves that form cusps due to the reflection or refraction of the rays at a curved surface. The mathematical description of these intensity patterns has been a subject of study since the time of Huygens (1690) and continues to be relevant today [38].

Inspired by these naturally occurring structures, modern optics enables the laboratory generation of structured light beams with intensity patterns that, like the caustics in a coffee cup, follow the Pearcey integral [39, 40]. These laboratory-generated beams, known as Pearcey-Gauss beams, exhibit remarkable properties such as auto-focusing, where the beam naturally concentrates at a high-intensity point without the need for

external lenses [41]. Additionally, these beams possess the extraordinary property of self-healing: even if an obstacle partially blocks their propagation, the beam can reconstruct itself and recover its original shape further along its path [40]. Recently, for the first time, vectorial Pearcey-Gauss beams were generated [23]. This section describes the experimental setup and methodologies used to generate and characterize these beams.

3.1.1 Mathematical framework

The Vortex Pearcey-Gauss (VPeG) beams can be represented at the initial plane $z = 0$ as [42, 43]

$$\mathrm{PeG}_{\ell}(x, y, 0) = \exp\left(-\frac{\rho^2}{w_0^2}\right) \mathrm{Pe}\left(\frac{x}{x_0 w_0}, \frac{y}{y_0 w_0}\right) \exp(i\ell\varphi), \tag{3.1}$$

where (x, y) and (ρ, φ) denote Cartesian and polar coordinates, respectively, w_0 is the beam waist of the Gaussian envelope, and ℓ corresponds to the topological charge. The function $\mathrm{Pe}(\cdot)$ represents the Pearcey integral, which determines the beam's structural characteristics [40].

A vectorial version of the VPeG beam is generated by modifying its polarization structure when passing it through a q-plate. As a result, the vectorial Vortex Pearcey-Gauss (VVPeG) beam is formulated as

$$\vec{E}(\vec{r}_{\perp}, 0) = \alpha\, \mathrm{PeG}_{\ell=2q}(\vec{r}_{\perp}, 0)\, \hat{e}_L + \beta\, \mathrm{PeG}_{\ell=-2q}(\vec{r}_{\perp}, 0)\, \hat{e}_R, \tag{3.2}$$

where α and β are complex coefficients constrained by $|\alpha|^2 + |\beta|^2 = 1$, $\vec{r}_{\perp}$ is the transverse position vector, and q is the charge of the q-plate [23].

3.1.2 Experimental setup

The experimental realization of VPeG and VVPeG beams is achieved through an optical setup that integrates a SLM and a q-plate, as depicted schematically in Fig. 3.1. The initial beam is horizontally polarized and originates from a Helium-Neon laser ($\lambda = 633$ nm). To ensure a well-defined input wavefront, the beam undergoes expansion and collimation through lenses L_1 and L_2. A variable aperture (A) selects the beam section to be utilized, which is then directed through a telescope system formed by lenses L_3 and L_4 (focal lengths of 200 mm). This setup precisely images the beam onto the reflective liquid crystal SLM (Holoeye Pluto 2.1 Phase Only LCOS), which features a pixel resolution of 1920×1080 and a pixel size of 8 μm. The SLM displays a computer-generated hologram that encodes the phase information required for PeG beam generation. The intended Pearcey-Gauss beam appears in the first diffraction

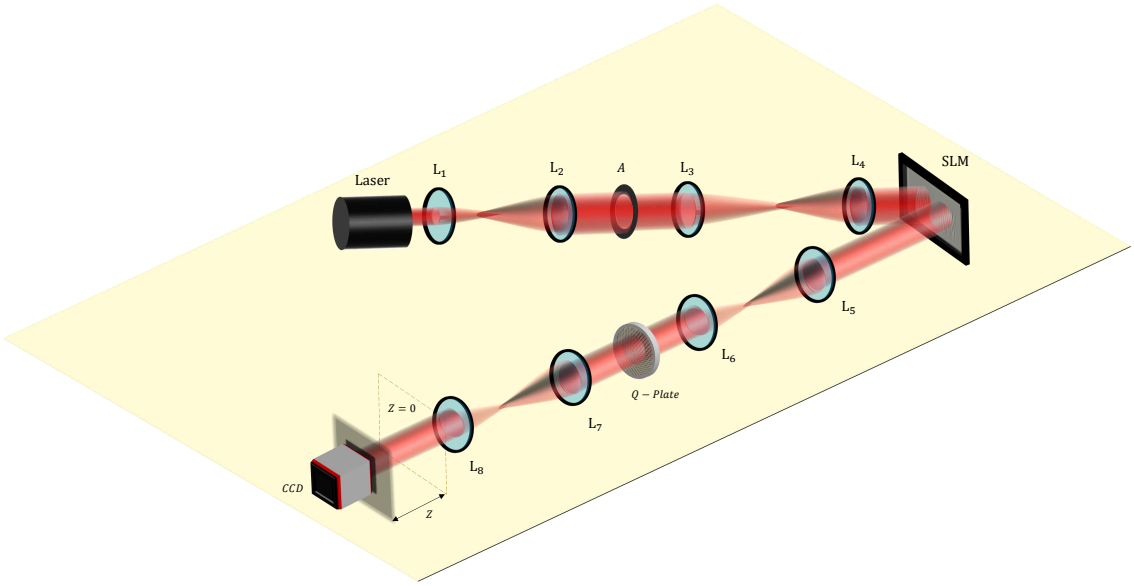

Figure 3.1: Experimental setup for generating Scalar and Vector Vortex Pearcey-Gauss beams. Here, an expanded and collimated laser beam with horizontal polarization impinges on an SLM, where the hologram to generate a Pearcey-Gauss beam is displayed. The plane of the SLM is imaged with a $4f$ system to coincide with the plane of a q-plate, which generates the VPeG or VVPeG beam. Another $4f$ system relays the plane of the q-plate to our plane $z = 0$. The intensity distribution of the beam is captured with a CCD camera mounted on a translation stage.

order. To extract the desired beam while filtering out unwanted diffraction orders, a spatial filtering stage is employed using a $4f$ optical system consisting of lenses L_5 and L_6 (focal lengths of $300\,$mm). A spatial filter at their Fourier plane removes residual light, producing a clean PeG beam. This $4f$ system also serves as an imaging stage, relaying the beam onto the q-plate. The q-plate subsequently transforms the beam into either a VPeG or a VVPeG beam, depending on its input polarization. A secondary $4f$ system, comprising lenses L_7 and L_8 (focal lengths of $150\,$mm), transmits the beam to the focal plane of L_8, establishing the reference plane $z = 0$. This configuration ensures that beam properties are analyzed in a well-defined optical plane. To record and analyze the generated beams, a CCD camera (DCX Thorlabs, with a pixel size of $4.65\ \mu$m) is positioned on a translation stage, enabling precise scanning along the propagation axis. Additionally, for far-field imaging, a lens with a focal length $f_9 = 300\,$mm (not shown in Fig. 3.1 for clarity) is included. This lens is placed at a distance $f_8 + f_9$ from L_8, with the CCD camera positioned f_9 beyond it, facilitating the observation of the beam's far-field intensity distribution.

3.1.3 Results

The study of VPeG and VVPeG beams involves examining their intensity distributions and polarization structures as they propagate. Initially, we analyze scalar VPeG beams by observing their intensity profiles at various propagation distances. Subsequently, we investigate the behavior of VVPeG beams by focusing on their polarization distribution, both in the near-field and at the far-field. We begin by constructing a horizontally polarized Pearcey-Gauss beam, which is then decomposed into its right- and left-handed circularly polarized components. By applying conjugated spiral phase distributions to these components, we introduce an optical vortex within the beam structure. Unlike previous works where the vortex was positioned at the primary intensity lobe [44, 45], here it is deliberately placed in the direction of the beam's natural propagation shift. As

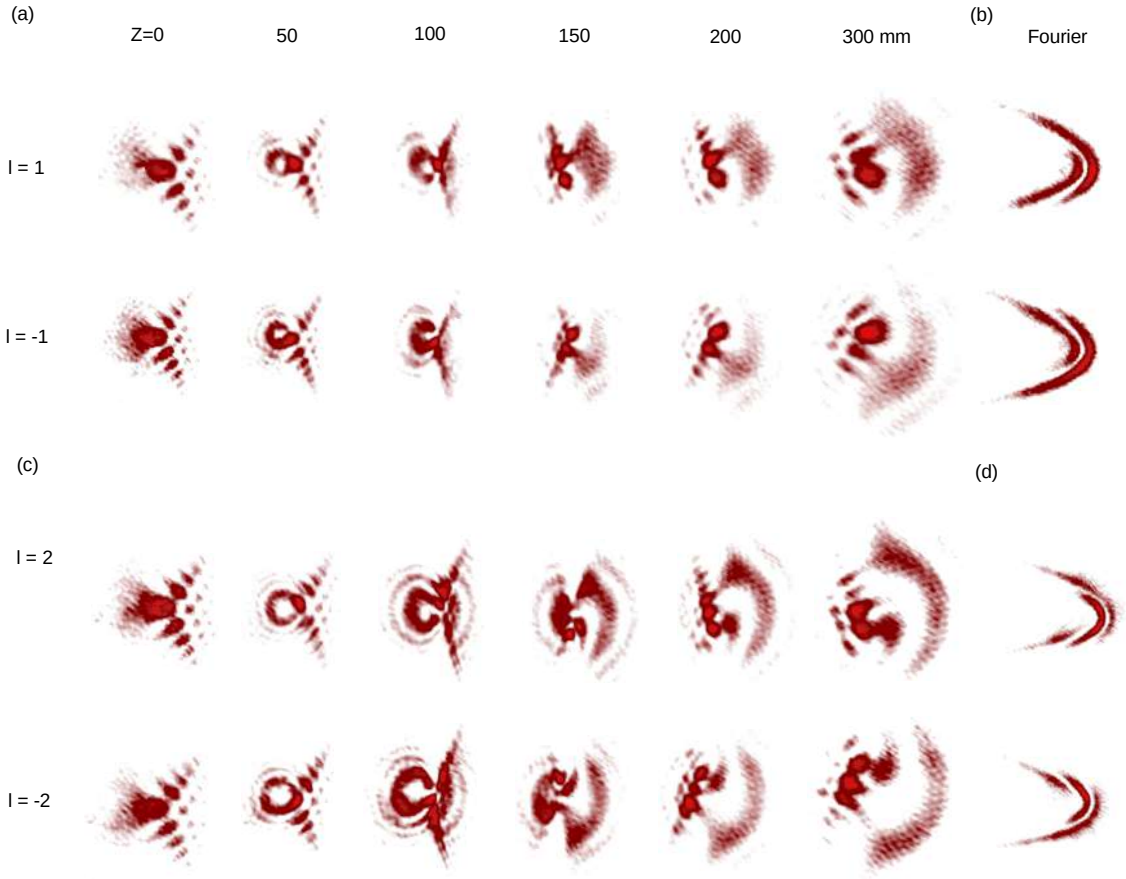

Figure 3.2: Intensity evolution of a VPeG beam as it propagates along the z-direction. (a) shows the results for $\ell = 1$ (top) and $\ell = -1$ (bottom), with the corresponding far-field (Fourier) distributions shown in (b). Similarly, (c) shows the results for $\ell = 2$ and $\ell = -2$, top and bottom, respectively, with the far-field distributions shown in (d).

the beams propagate, notable changes occur in their intensity patterns, as shown in Figure 3.2. For a topological charge of $\ell = 1, 2$, the initial distribution resembles a standard Pearcey-Gauss beam. However, as propagation advances, a dark core emerges at the vortex location, reflecting the phase singularity where intensity must vanish. The primary intensity lobe appears to orbit around this dark core before redistributing asymmetrically at longer distances. Additionally, the intensity profiles for opposite charges are mirror reflections of each other, highlighting the influence of vortex handedness on the resulting beam structure.

Extending this analysis to VVPeG beams, we generate these fields using a combination of a SLM and a q-plate, ensuring that the generated beams exhibit inhomogeneous polarization states. Unlike their scalar counterparts, the intensity patterns of VVPeG beams remain symmetric along the horizontal axis. This symmetry arises be-

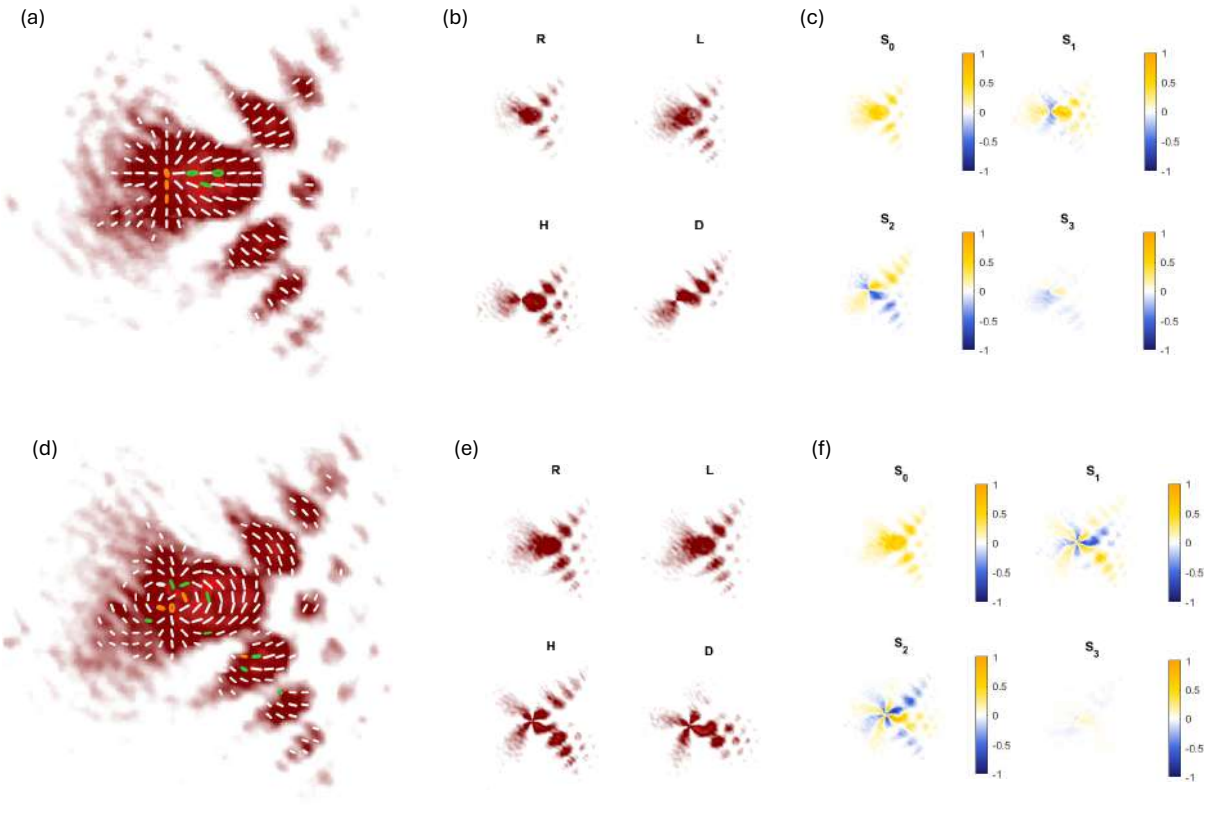

Figure 3.3: Reconstructed transverse polarization patterns of two VVPeGs are shown in (a) and (d). (b,e) Measured intensity distributions in circular (R, L), linear horizontal (H), and diagonal (D) polarization bases. (c,f) Corresponding normalized Stokes parameters S_0, S_1, S_2, and S_3, providing a complete mapping of the polarization state. The top row (a–c) and bottom row (d–f) correspond to two different VVPeGs, the first with topological charge $\ell = 1$, and the second with $\ell = 2$.

cause the total intensity results from the sum of the two polarization components, which are mirror images of one another. The initial polarization distribution is predominantly linear, but as the beam propagates, additional elliptical and circular polarization states emerge. By the time the beam reaches longer propagation distances, the polarization distribution closely resembles that of a full Poincaré beam, where a diverse range of polarization states coexist within a single transverse profile.

In the far-field regime, the intensity distributions of VVPeG beams feature complete parabolic structures, rather than the semi-parabolic patterns observed in scalar cases.

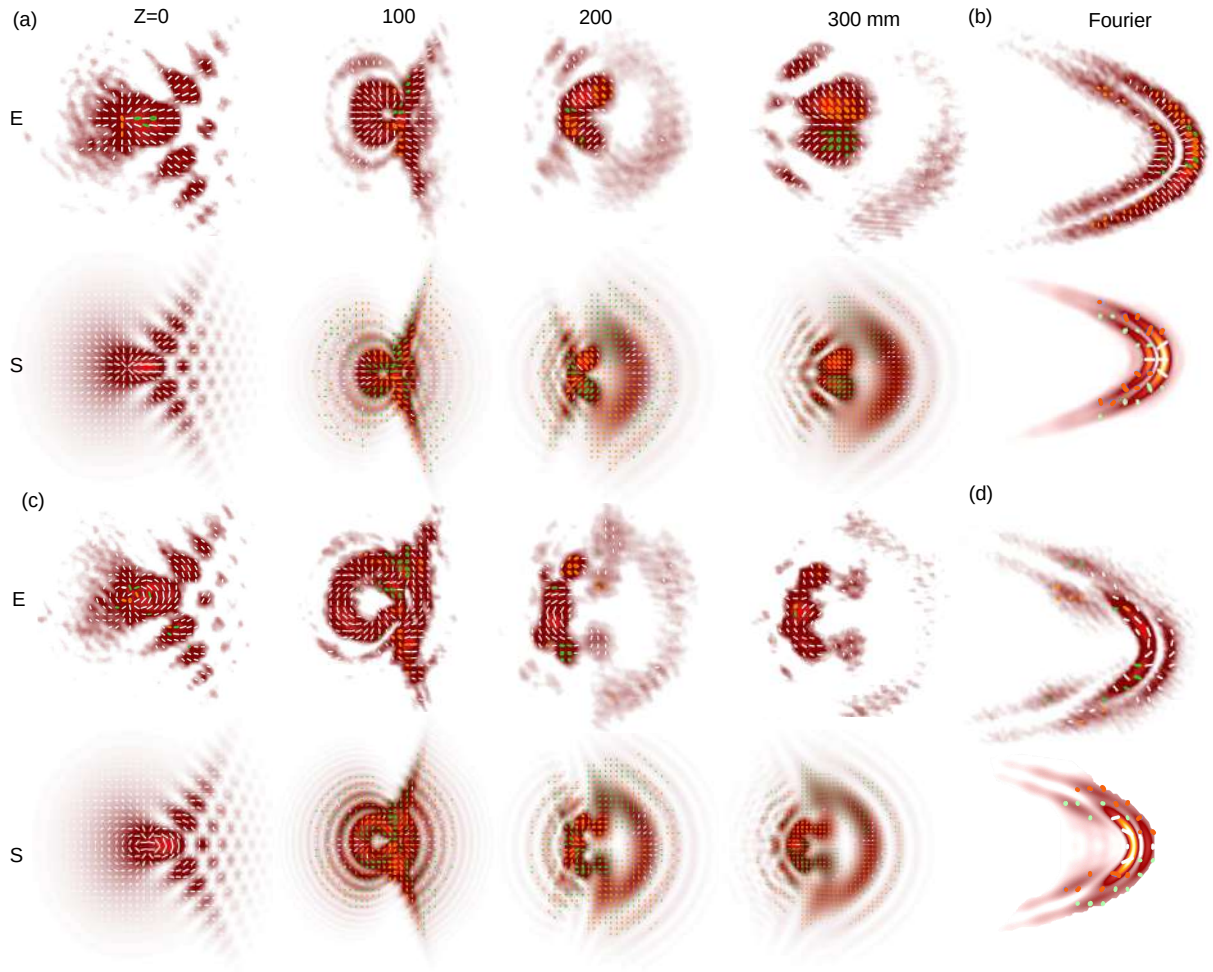

Figure 3.4: Transverse polarisation distributions overlapped with the intensity profiles of vector vortex Pearcey (VVPeG) beams at various planes along the propagation direction. (a),(b) and (c),(d) correspond to VVPeG beams with left- and right-handed polarisation components of topological charges $\ell = \pm 1$ and $\ell = \pm 2$, generated using q-plates with $q = 1/2$ and $q = 1$, respectively. Experiments (E) are on top and numerical simulations (S) are on the bottom. (b),(d) correspond to the results in the far-field. Blue and green ellipses represent right- and left-handed circular polarisation, respectively, and white lines represent linear polarisation.

The polarization evolves from an initial radial-like configuration to more complex distributions, revealing intricate polarization topologies that depend on the beam parameters.

3.2 Experimental implementation of curvilinear polarization vector beams

We implemented the experimental setup shown in Fig. 3.5 to generate spatially varying polarization structures aligned with curvilinear directions [46]. A diagonally polarized HeNe laser beam served as the input source. After beam expansion and collimation, producing a beam with a $2\ \mathrm{mm}$ radius, the field uniformly illuminated a phase-only SLM (Holoeye Pluto VIS, $8\ \mu\mathrm{m}$ pixel pitch, calibrated at $633\ \mathrm{nm}$).

The SLM modulates only the horizontal polarization component. In the linear basis, its action can be modeled by the Jones matrix:

$$\mathbf{J}_{\text{SLM}} = \begin{bmatrix} e^{i\theta_h(\mathbf{r})} & 0 \\ 0 & 1 \end{bmatrix}, \tag{3.3}$$

where $\theta_h(\mathbf{r})$ is a computer-generated phase pattern applied solely to the horizontal polarization [47, 48].

A QWP oriented at 45° follows the SLM and converts the horizontal component into right-circular polarization ($\hat{e}_R$), while the vertical component becomes left-circular polarization ($\hat{e}_L$).

To synthesize a polarization field aligned with a desired local direction $\hat{e}_u(\mathbf{r})$, we express the transverse unit vectors in the circular polarization basis as

$$\begin{aligned} \hat{e}_u(\mathbf{r}) &= \frac{1}{\sqrt{2}}\left(\hat{e}_L + e^{i2\theta_u(\mathbf{r})}\hat{e}_R\right), \\ \hat{e}_v(\mathbf{r}) &= \frac{1}{\sqrt{2}}\left(\hat{e}_L - e^{i2\theta_u(\mathbf{r})}\hat{e}_R\right), \end{aligned} \tag{3.4}$$

where $\theta_u(\mathbf{r})$ determines the local orientation of the polarization ellipse. These vectors are everywhere orthonormal and allow full control over the polarization distribution through the phase $2\theta_u(\mathbf{r})$.

Given that the QWP converts horizontal polarization into $\hat{e}_R$, we generate the desired structure by encoding

$$\theta_h(\mathbf{r}) = -2\theta_u(\mathbf{r})$$

onto the SLM. This induces the appropriate phase shift in the right-circular component,

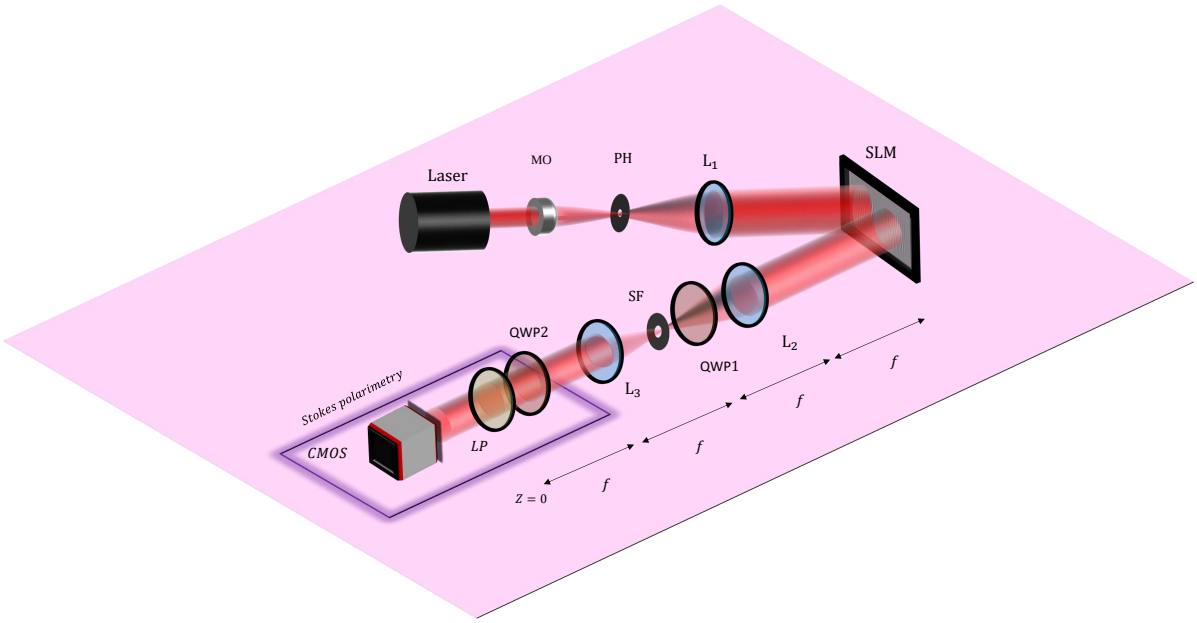

Figure 3.5: Experimental setup for the generation and analysis of spatially varying polarization structures. A diagonally polarized HeNe laser is expanded and collimated using a microscope objective (MO), a pinhole (PH), and a lens (L_1), before illuminating a phase-only SLM. The modulated beam passes through a QWP1 that transforms the linear basis into the circular basis. A 4f system composed of lenses L_2 and L_3 relays the beam to the analysis plane ($z = 0$), where spatially resolved Stokes polarimetry is performed using a rotatable QWP2, a LP, and a CMOS camera.

resulting in the superposition described by Eq. 3.4.

The modulated beam is then relayed to the detection plane through a 4f imaging system. To analyze the resulting polarization distribution, we perform spatially resolved Stokes polarimetry by acquiring six intensity projections (H, V, D, A, R, L). From these measurements, the Stokes parameters are reconstructed, allowing full characterization of the polarization state across the beam. We construct polarization bases aligned with four representative curvilinear geometries: elliptical, parabolic, bipolar, and dipole coordinate systems. For each case, we specify the coordinate transformation, identify the corresponding conformal map, and derive the spatially varying phase required in Eq. 3.4 to express the basis in the circular polarization representation.

3.2.1 Elliptical Polarization Bases

The elliptical coordinate system is defined through the transformation

$$\begin{aligned} x &= a\cosh u\cos v, \\ y &= a\sinh u\sin v, \end{aligned} \tag{3.5}$$

where $a > 0$ places the two foci at $(x, y) = (\pm a, 0)$. The associated conformal map,

$$z = a\cosh w, \tag{3.6}$$

is one-to-one with $w = u + iv$ and domain $u \in [0, \infty)$, $v \in [0, \pi]$. In this geometry, curves of constant u correspond to confocal ellipses, while curves of constant v correspond to confocal hyperbolas. A branch cut appears at $u = 0$, connecting the two foci along the x-axis, where the metric becomes singular.

The polarization basis defined in Eq. (3.4) can be adapted to this coordinate system by introducing a spatially varying phase

$$\theta_u = arctan\left(\coth u\ \tan v\right), \tag{3.7}$$

which aligns the local polarization vectors with the elliptical and hyperbolic coordinate lines.

Experimentally, the semi-focal distance a plays a crucial role in controlling the polarization modulation across the beam profile. For large values of a, the polarization distribution tends to be nearly uniform, and the influence of the elliptical structure is suppressed. Conversely, decreasing a enhances the curvilinear features, leading to polarization patterns that closely follow the underlying coordinate curves.

Figure 3.6 shows the experimental results obtained with the optical setup described previously. Panels (a)–(d) correspond to the case where the coordinate u was kept constant, leading to polarization patterns aligned with confocal ellipses. Panels (e)–(h) correspond to the case where v was kept constant, producing polarization structures aligned with confocal hyperbolas. In each case, the reconstructed polarization vectors are overlaid on the intensity profile S_0, and the corresponding normalized Stokes parameters S_1, S_2, and S_3 are presented for one of the polarization patterns according to the coordinate that was held fixed.

The influence of the foci separation is further constrained by the spatial resolution of the SLM used in the experiment. Our SLM features 1920 pixels with a pixel pitch of $8\ \mu\mathrm{m}$. When the total distance between the foci $(2a)$ matches the width of the SLM,

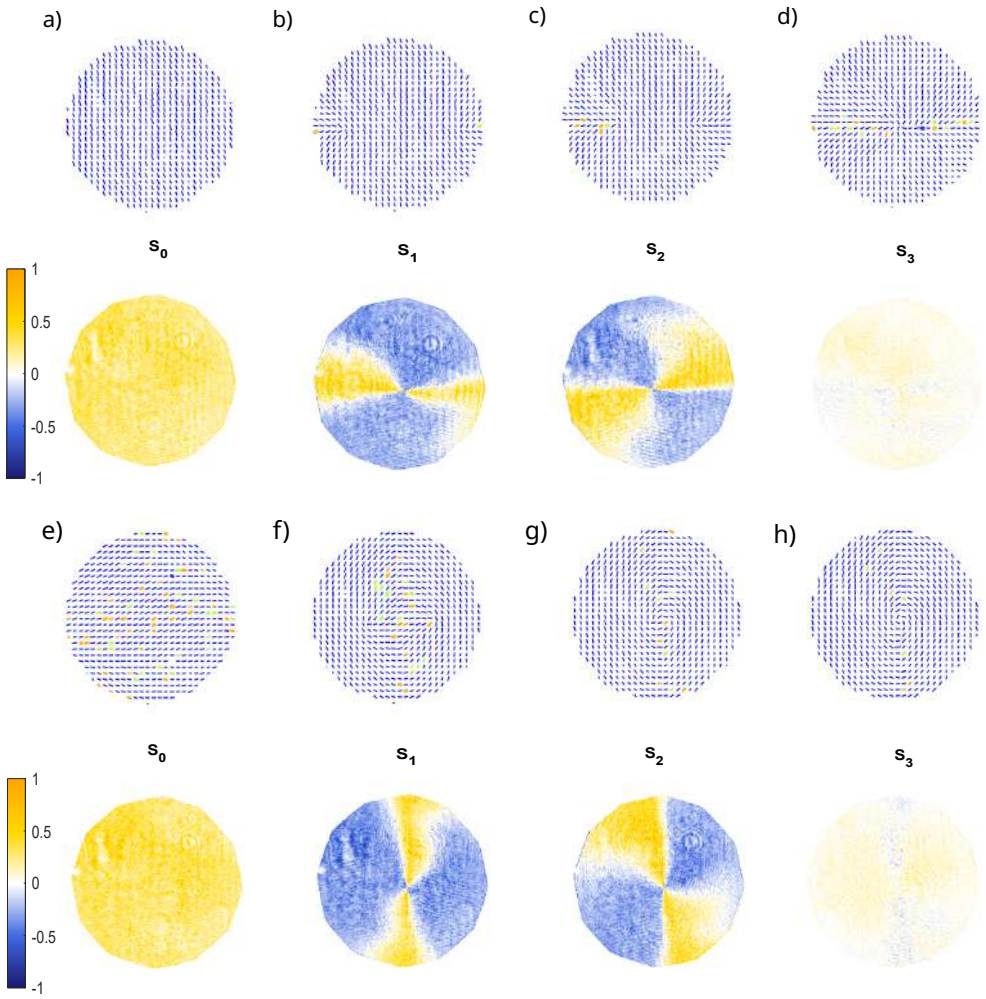

Figure 3.6: Experimental polarization distributions obtained with the described optical setup. (a)–(d) Reconstructed polarization vectors over the intensity profile S_0 and the corresponding normalized Stokes parameters S_1, S_2, and S_3. (e)–(h) Similar measurements for a different semi-focal distance a. The results demonstrate the emergence of polarization structures aligned with the elliptical and hyperbolic coordinate lines as the parameter a is varied.

the resulting beam exhibits a scalar polarization profile without singularities, as seen in previous observations. As a increases, the beam undergoes a gradual transition from scalar to vectorial, developing structured polarization distributions with either radial or azimuthal symmetry, depending on the encoded phase pattern.

3.2.2 Parabolic Coordinate System

The parabolic coordinate system is defined through the transformation

$$\begin{aligned} x &= \frac{1}{2}\left(u^2 - v^2\right), \\ y &= uv, \end{aligned} \tag{3.8}$$

where $u \in [0, \infty)$ and $v \in (-\infty, \infty)$. In this geometry, curves of constant u correspond to parabolas opening to the left, while curves of constant v correspond to parabolas opening to the right. The conformal map remains regular throughout the domain except at $w = 0$, corresponding to the Cartesian origin, where the scale factors vanish. Although the forward map is continuous, its inverse $w = \sqrt{2z}$ requires a branch cut.

The local polarization basis can be constructed using the spatially varying phase

$$\theta_u = \arctan\left(\frac{v}{u}\right), \tag{3.9}$$

which aligns the polarization vectors along the coordinate curves. As a result, the electric field orientation follows the orthogonal families of parabolas opening in opposite directions.

The experimental results obtained with the optical setup described previously are

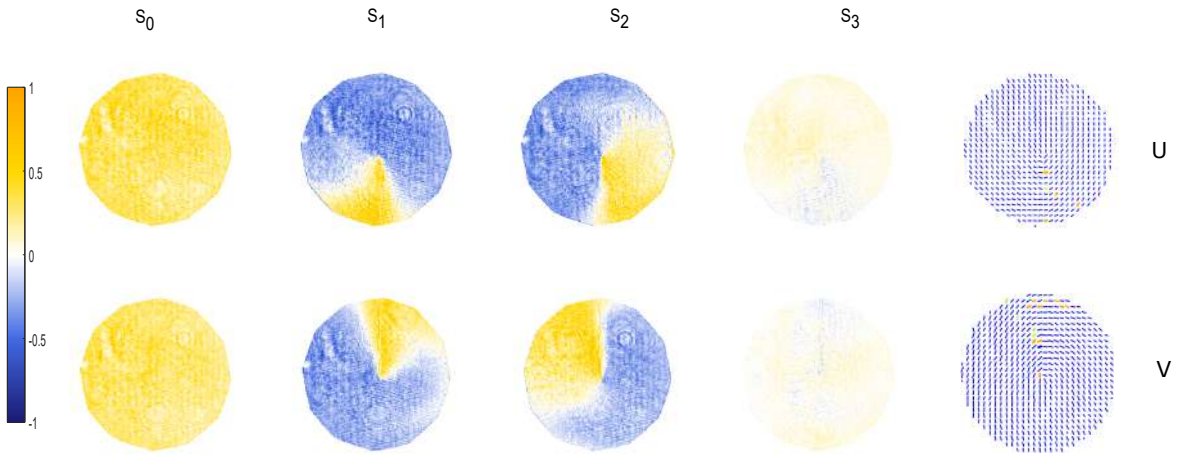

Figure 3.7: Experimental polarization patterns structured according to parabolic coordinates. The first row shows results for a polarization field aligned along curves of constant u (left-opening parabolas), and the second row corresponds to alignment along curves of constant v (right-opening parabolas). Columns from left to right display the normalized Stokes parameters S_0, S_1, S_2, and S_3, followed by the reconstructed polarization vectors.

presented in Fig. 3.7. The first row corresponds to the polarization distribution constructed by keeping u constant, associated with parabolas opening to the left. The second row shows the distribution obtained by maintaining v constant, corresponding to parabolas opening to the right. For each case, the polarization vectors are shown alongside the spatial distributions of the normalized Stokes parameters S_0, S_1, S_2, and S_3.

3.2.3 Bipolar Coordinate System

The bipolar coordinate system is defined through the transformation

$$\begin{aligned} x &= a\frac{\sinh v}{\cosh v - \cos u}, \\ y &= a\frac{\sin u}{\cosh v - \cos u}, \end{aligned} \tag{3.10}$$

where $a > 0$ positions the two foci at $(x, y) = (\pm a, 0)$. In this geometry, curves of constant u form non-concentric circles centered along the y-axis at $(0, a\cot u)$ with radius $a/\sin u$, while curves of constant v form non-intersecting circles centered at $(a\coth v, 0)$ with radius $a/\sinh v$. These two families of circles intersect orthogonally at the foci. A branch cut appears along the segment joining the foci on the x-axis, corresponding to $u = 0$, and the metric becomes singular at each focal point.

The local orientation of the polarization can be described by the spatially varying phase

$$\theta_u = \arctan\left(\frac{\cosh v\, \cos u - 1}{\sinh v\, \sin u}\right), \tag{3.11}$$

which encodes the geometry of the bipolar coordinate system, aligning the polarization vectors with the orthogonal families of circular arcs.

The semi-focal distance a plays a crucial role in shaping the polarization structure across the transverse plane. For large values of a, the polarization tends toward a uniform distribution, diminishing the influence of the curvilinear structure. As a decreases, the underlying geometry becomes more prominent, and the polarization vectors increasingly follow the bipolar coordinates.

Figure 3.8 shows the experimental results obtained with the optical setup described previously. Panels (a)–(d) correspond to the case where the coordinate u was kept constant, resulting in polarization patterns aligned with families of non-intersecting circular arcs characteristic of the bipolar coordinate system. Panels (e)–(h) correspond to the case where v was kept constant, generating polarization structures aligned with inter-

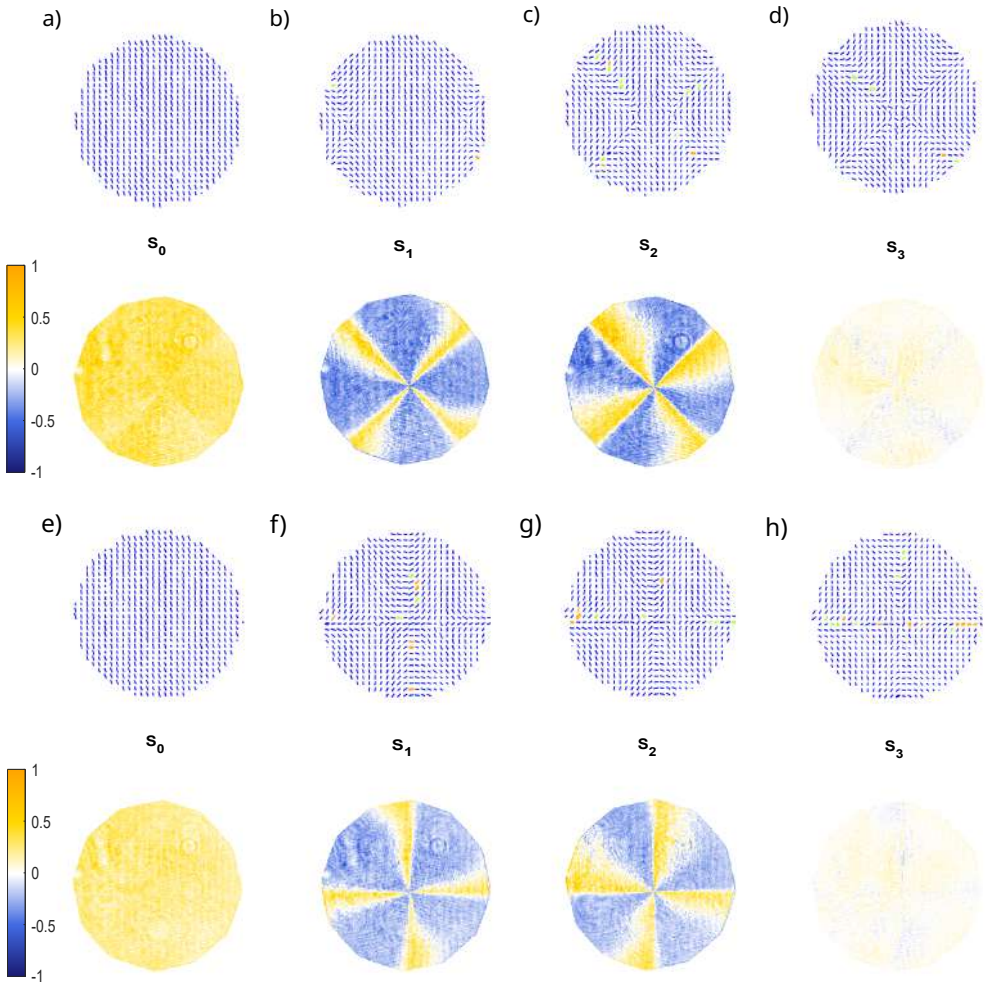

Figure 3.8: Experimental polarization distributions obtained with the described optical setup. (a)–(d) Reconstructed polarization vectors over the intensity profile S_0 and the corresponding normalized Stokes parameters S_1, S_2, and S_3 for one family of bipolar coordinate curves. (e)–(h) Similar measurements for the orthogonal family of curves. The results demonstrate the emergence of polarization structures aligned with the intersecting and non-intersecting circular arcs characteristic of the bipolar coordinate system as the parameter a is varied.

secting circular arcs. In each case, the reconstructed polarization vectors are overlaid on the intensity profile S_0, and the corresponding normalized Stokes parameters S_1, S_2, and S_3 are shown for one of the polarization patterns, depending on which coordinate was held fixed.

3.2.4 Dipole Coordinate System

The dipole coordinate system is defined by the transformation

$$\begin{aligned} x &= \frac{u}{u^2+v^2}, \\ y &= -\frac{v}{u^2+v^2}, \end{aligned} \tag{3.12}$$

where u and v are real variables. The associated conformal map,

$$z = \frac{1}{w}, \tag{3.13}$$

with $w = u + iv$, is one-to-one within the domain $u \in (-\infty, 0) \cup (0, \infty)$ and $v \in (-\infty, 0) \cup (0, \infty)$. In this geometry, curves of constant u correspond to non-concentric circles centered at $(x, y) = (u/2, 0)$, while curves of constant v are non-concentric circles centered at $(x, y) = (0, -v/2)$. Although the conformal map does not introduce a branch cut, it becomes singular at $w = 0$, corresponding to the origin in Cartesian coordinates, where the scale factors diverge.

The polarization basis defined in Eq. (3.4) can be expressed through a spatially

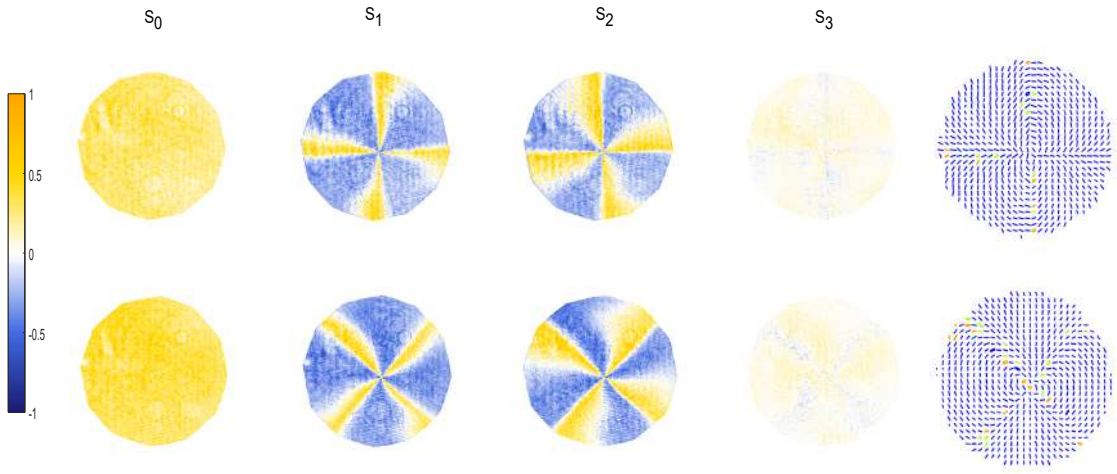

Figure 3.9: Experimental polarization patterns structured according to dipolar coordinates. The first row shows results for a polarization field aligned along curves of constant u (non-concentric circles centered along the x-axis), and the second row corresponds to alignment along curves of constant v (non-concentric circles centered along the y-axis). Columns from left to right display the normalized Stokes parameters S_0, S_1, S_2, and S_3, followed by the reconstructed polarization vectors.

varying phase,

$$\theta_u = \arctan\left(\frac{2uv}{v^2 - u^2}\right), \tag{3.14}$$

which encodes the local geometry of the dipole coordinate system. This phase determines linear polarization orientations that follow the orthogonal families of non-concentric circles. In the dipole coordinate system, the polarization distribution follows the orthogonal families of non-concentric circles defined by the conformal map $z = 1/w$. Due to the nature of this mapping, angular variations become concentrated near the origin, resulting in high spatial gradients in the polarization field.

The experimental results obtained with the optical setup described previously are presented in Fig. 3.9. The first row corresponds to the polarization distribution constructed by keeping u constant, resulting in polarization aligned along non-concentric circles centered along the x-axis. The second row shows the distribution obtained by maintaining v constant, where the polarization aligns with non-concentric circles centered along the y-axis. For each case, the reconstructed polarization vectors are displayed alongside the spatial distributions of the normalized Stokes parameters S_0, S_1, S_2, and S_3.

4 | The effect of Dove prism on vector beams

There are several types of reflective prisms, such as the corner cube [49], the pentaprism [50], the Amici prism [51], the rhomboid prism, the Pechan prism [52], and the DP [53]. These prisms are designed to prevent light dispersion by taking advantage of the phenomenon of total internal reflection, which gives them a wide range of applications. Among the basic ones are image formation, interferometers, laser cavities, polarimeters, and others [54]. The DP, in addition to being a reflective prism, is also the simplest inverting-reversing prism, as it achieves image inversion and rotation (by twice the angle) with just one reflection, without altering the propagation direction [55, 56]. This effect is illustrated in Figure 4.1, which shows the projection of points forming the image of the letter **R** on the entrance surface of the prism and the resulting

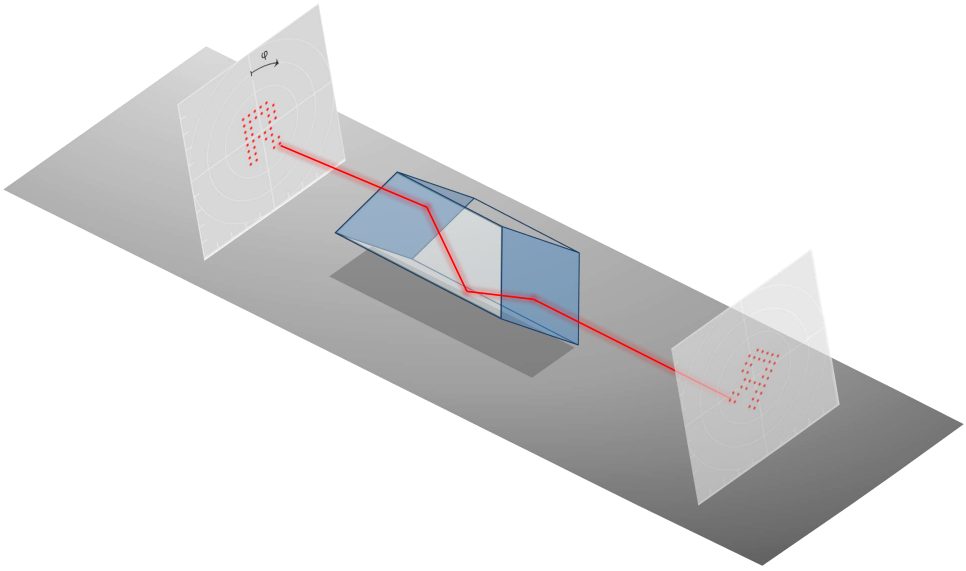

Figure 4.1: The DP rotates an image by twice the angle at which the prism itself is rotated. If an image enters a DP rotated by an angle $\phi = 22.5°$, the resulting image exiting the prism will be rotated by $45°$ and inverted.

image after propagation through the prism, projected onto a hypothetical plane at the exit. Although the DP is rotated by only $\phi = 22.5°$, the letter **R** undergoes both inversion and a $45°$ rotation.

In addition to the characteristics mentioned so far, it has been reported that this prism affects polarization and OAM [57]. This is of great interest when working with vector beams, and thus, the remainder of this chapter focuses on describing these effects. In experimental setups involving vector beams and DPs, it is common to neglect either the polarization or spatial mode transformations induced by the prism. However, there is still a lack of clarity regarding the actual impact of DP on beams with coupled DoFs. Some studies treat the DP as acting solely on the OAM of the beam [58], while others emphasize its influence on polarization [59]. The aim of this work is to unambiguously determine the real effect of the DP on vector beams and to identify under which conditions its action on both DoFs can be safely neglected.

4.1 The effect of a rotating Dove prism on scalar beams: Polarization

When a light beam passes through a DP, it interacts with three of its surfaces. The changes in the electric field, resulting from these interactions, can be represented by Jones matrices that depend only on the Fresnel coefficients and the prism's rotation angle. These matrices allow us to analyze the effect of DPs on the polarization state of a beam.

For a beam with vertical linear polarization, it is observed that if the prism is not rotated, the polarization remains unchanged. However, as the prism rotates, the polarization gradually becomes more elliptical, reaching its maximum ellipticity at a rotation angle of $\phi = \frac{\pi}{4}$. Beyond this point, the ellipticity decreases, returning to its initial state at $\phi = \frac{\pi}{2}$. This behavior repeats as the prism continues to rotate, completing a cycle at $\phi = 2\pi$. The formalism used to find the Jones matrices representing such an effect will be briefly discussed below, as illustrated in Figure 4.2.

4.1.1 Jones matrix of a Dove prism for polarization

A beam propagating in the direction $\mathbf{k_i}$ impinges on one of the surfaces of the reflective prism and refracts upon passing through it. Inside the prism, the refracted beam strikes a second surface, where it undergoes internal reflection, as illustrated in *Figure 4.1*. The beam then continues its propagation, redirecting toward a third surface. At each refraction and reflection, the s-p coordinate system shifts relative to the original axis,

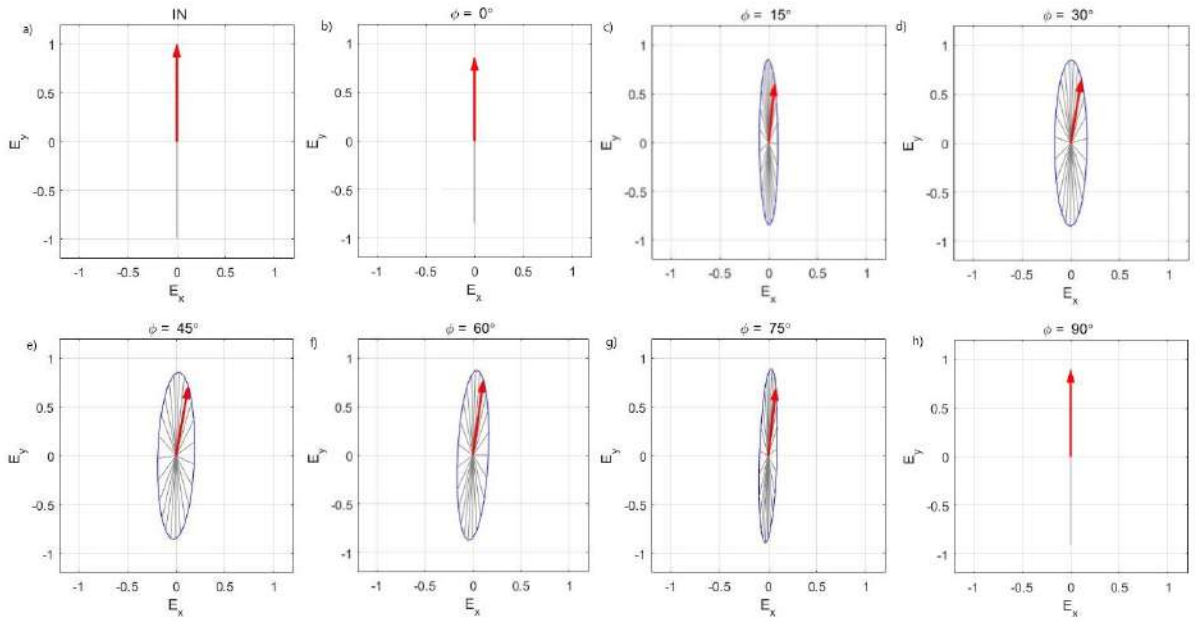

Figure 4.2: Illustration of polarization transformations in the electric field induced by DP rotation: (a) incident beam, (b) zero rotation, (c) $15°$, (d) $30°$, (e) $45°$, (f) $60°$, (g) $75°$, and (h) $90°$ rotations. As the prism rotates, the field amplitude is modulated during propagation, accompanied by changes in the polarization state

causing the electric field to modify its associated polarization states. These changes are analyzed using a transformation matrix system to represent the fields and their interactions.

The process of determining the transformation matrices begins by expressing the electric field $\mathbf{E}$ of a beam incident on a prism as a linear combination of the orthonormal

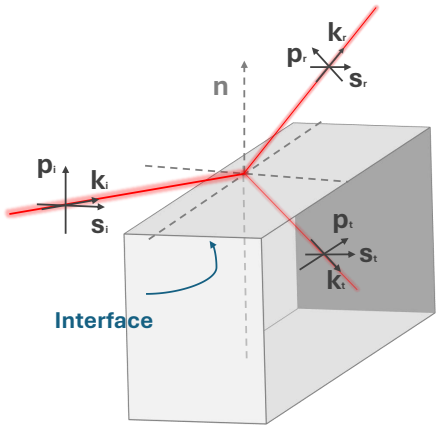

Figure 4.3: A ray with coordinates (s_i, p_i, k_i) strikes a prism, generating a transmitted ray with coordinates (s_t, p_t, k_t) and a reflected ray with coordinates (s_r, p_r, k_r).

basis vectors $\mathbf{s_i}$, $\mathbf{p_i}$, and $\mathbf{k_i}$, as shown in *Figure 4.3*:

$$\mathbf{E} = (\mathbf{E} \cdot \mathbf{p_i})\mathbf{p_i} + (\mathbf{E} \cdot \mathbf{s_i})\mathbf{s_i}. \tag{4.1}$$

In this context, the special condition of electromagnetic propagation is considered when $\mathbf{E} \cdot \mathbf{k_i} = 0$, and $\mathbf{s_i}$ and $\mathbf{p_i}$ are defined as follows:

$$\mathbf{p_i} = \mathbf{s_i} \times \mathbf{k_i}, \quad \text{and} \quad \mathbf{s_i} = \frac{\mathbf{k_i} \times \mathbf{n_i}}{|\mathbf{k_i} \times \mathbf{n_i}|}, \tag{4.2}$$

where $\mathbf{n_i}$ is the normal vector to the i-th surface, and $\mathbf{k_i}$ is the propagation vector.

Depending on whether the interaction between the beam and the prism corresponds to a reflection or a transmission process, the resulting electric field is determined using one of the following expressions based on the Fresnel coefficients. In the case of transmission, the electric field is modified according to the following.

$$\mathbf{E_{(final)t}} = \; t_{m\parallel}(\mathbf{E_{m-1}} \cdot \mathbf{p_m})\; \mathbf{p_m} \; + \; t_{m\perp}(\mathbf{E_{m-1}} \cdot \mathbf{s_m})\; \mathbf{s_m}, \tag{4.3}$$

whereas, for reflection, the electric field is given by:

$$\mathbf{E_{(final)r}} = \; r_{n\parallel}(\mathbf{E_{n-1}} \cdot \mathbf{p_n})\; \mathbf{p_n} \; + \; r_{n\perp}(\mathbf{E_{n-1}} \cdot \mathbf{s_n})\; \mathbf{s_n}. \tag{4.4}$$

The subscripts m and n will be assigned values according to the surface being studied. Specifically, if a reflection on the second surface of a prism is being analyzed, the equation that describes how the electric field changes when interacting with that surface will be Eq. (4.4), where the subscript n will take the value of the surface number, $n = 2$. The appearance of the letters r, and t in the subscripts simply indicates whether the vector is associated with the reflected, or transmitted beam, respectively.

For both reflection and transmission, this effect can be represented in matrix form as shown below:

$$\begin{bmatrix} E_{(final)\parallel t} \\ E_{(final)\perp t} \end{bmatrix} = \begin{bmatrix} t_{m\parallel}\,(\mathbf{p_{m-1}} \cdot \mathbf{p_m}) & t_{m\parallel}\,(\mathbf{s_{m-1}} \cdot \mathbf{p_m}) \\ t_{m\perp}\,(\mathbf{p_{m-1}} \cdot \mathbf{s_m}) & t_{m\perp}\,(\mathbf{s_{m-1}} \cdot \mathbf{s_m}) \end{bmatrix} \begin{bmatrix} E_{(m-1)\parallel} \\ E_{(m-1)\perp} \end{bmatrix}, \tag{4.5}$$

$$\begin{bmatrix} E_{(final)\parallel r} \\ E_{(final)\perp r} \end{bmatrix} = \begin{bmatrix} r_{n\parallel}\,(\mathbf{p_{n-1}} \cdot \mathbf{p_n}) & r_{n\parallel}\,(\mathbf{s_{n-1}} \cdot \mathbf{p_n}) \\ r_{n\perp}\,(\mathbf{p_{n-1}} \cdot \mathbf{s_n}) & r_{n\perp}\,(\mathbf{s_{n-1}} \cdot \mathbf{s_n}) \end{bmatrix} \begin{bmatrix} E_{(n-1)\parallel} \\ E_{(n-1)\perp} \end{bmatrix}. \tag{4.6}$$

In the case of the DP, the incident beam is transmitted through the first surface ($n = 1$), reflection on the second surface ($n = 2$), and transmission once again through

the third surface ($n = 3$). Consequently, the initial electric field $\mathbf{E_0}$ is sequentially transformed by the corresponding matrices associated with each interaction. These matrices depend on the prism's rotation angle ϕ, and the resulting field is expressed as:

$$\mathbf{E} = R\, t_3\, r_2\, t_1\, \mathbf{E_0}, \tag{4.7}$$

where t_1, r_2, and t_3 denote the Fresnel transmission and reflection matrices for each respective surface, and R is the rotation matrix used to return the field to the global rectangular coordinate basis. These matrices take the following explicit forms:

$$t_1 = \begin{bmatrix} t_{1\parallel}\, cos\, \phi & t_{1\parallel}\, sen\, \phi \\ -t_{1\perp}\, sen\, \phi & t_{1\perp}\, cos\, \phi \end{bmatrix}, \tag{4.8}$$

$$r_2 = \begin{bmatrix} r_{2\parallel} & 0 \\ 0 & r_{2\perp} \end{bmatrix}, \tag{4.9}$$

$$t_3 = \begin{bmatrix} -t_{3\parallel} & 0 \\ 0 & -t_{3\perp} \end{bmatrix}, \tag{4.10}$$

$$R = \begin{bmatrix} cos\, \phi & -sen\, \phi \\ sen\, \phi & cos\, \phi \end{bmatrix}. \tag{4.11}$$

As discussed in the chapter on structured light, it is common for vector beams to be expressed in a basis defined by two orthogonal polarizations, typically right- and left-circular polarization. On the other hand, we have just identified four matrices whose product results in a matrix representing the effect of the DP on an incident electric field. These matrices are defined in a basis consisting of s- and p-polarizations, making it necessary to perform the corresponding transformation. To bridge these representations, we employ the unitary transformation matrix S:

$$S = \frac{1}{\sqrt{2}} \begin{bmatrix} 1 & i \\ 1 & -i \end{bmatrix}. \tag{4.12}$$

The relationship between a matrix in the original basis and its representation in the transformed basis is given by $M' = SMS^{-1}$. So applying this transformation to each

DP matrix, we obtain the following matrices:

$$t_1' = \frac{1}{2}\begin{bmatrix} (t_{1\parallel} + t_{1\perp})e^{-i\phi} & (t_{1\parallel} - t_{1\perp})e^{i\phi} \\ (t_{1\parallel} - t_{1\perp})e^{-i\phi} & (t_{1\parallel} + t_{1\perp})e^{i\phi} \end{bmatrix}, \tag{4.13}$$

$$r_2' = \frac{1}{2}\begin{bmatrix} r_{2\parallel} + r_{2\perp} & r_{2\parallel} - r_{2\perp} \\ r_{2\parallel} - r_{2\perp} & r_{2\parallel} + r_{2\perp} \end{bmatrix}, \tag{4.14}$$

$$t_3' = \frac{1}{2}\begin{bmatrix} -t_{3\parallel} - t_{3\perp} & -t_{3\parallel} + t_{3\perp} \\ -t_{3\parallel} + t_{3\perp} & -t_{3\parallel} - t_{3\perp} \end{bmatrix}, \tag{4.15}$$

$$R' = \begin{bmatrix} e^{i\phi} & 0 \\ 0 & e^{-i\phi} \end{bmatrix}. \tag{4.16}$$

4.2 The effect of a rotating Dove prism on scalar beams: OAM

When analyzing a beam carrying OAM, additional spatial effects must be taken into account due to the unique helical structure of its wavefront. The analysis carried out so far in this chapter employs Fresnel coefficients to describe the interaction between the electric field and the surface of the prism. These coefficients are derived under the assumption that the wavefront of the electric field is planar, a condition that does not hold for beams carrying OAM. In the case of such beams, in order to apply Fresnel coefficients, the helical wavefront must be considered as a superposition of plane waves, each forming a specific angle with respect to the propagation direction of the beam, as illustrated in *Figure4.4 (a)* [60]. The inclination angle α_i is given by [61]:

$$\alpha_i = \arctan\left(\frac{l}{k\rho_i}\right), \tag{4.17}$$

where l is the topological charge of the beam, k is the wave number, defined as $k = 2\pi/\lambda$ with λ being the wavelength; and ρ_i is the radial distance from the beam axis at which the local plane wave approximation is evaluated. The angle α_i accounts for the local tilt of the wave vector due to the helical structure and must be subtracted from the nominal angle of incidence when computing the Fresnel coefficients for each

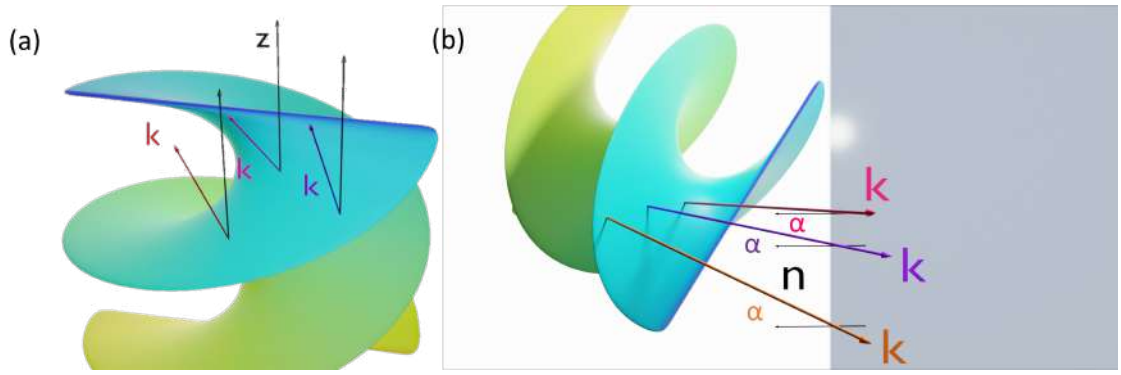

Figure 4.4: (a) Decomposition of an optical beam carrying OAM into plane waves, each forming an inclination angle α_i with respect to the beam's propagation direction ($\mathbf{z}$). The wave vectors ($\mathbf{k}$) corresponding to each hypothetical plane wave are shown. (b) Interaction of the OAM beam with an interface. The local inclination angle α_i modifies the effective incidence angle, requiring a correction when applying Fresnel coefficients. The angle θ_{in} denote the conventional incidence angle, while θ_{i} represent the incidence angle of each plane wave. $\mathbf{n}$ represents the surface normal.

component, as depicted in *Figure 4.4(b)*.

In addition, it is well known that when a light beam carrying OAM, described by

$$A_{\text{in}} = A(\rho)\exp(il\varphi),$$

propagates through a DP, the output field acquires a modified spatial structure given by [57, 62]

$$A_{\text{out}} = A(\rho)\exp(-il\varphi)\exp(-2il\phi).$$

In this expression, φ denotes the *azimuthal coordinate* in cylindrical coordinates, which characterizes the transverse phase structure of the beam, while ϕ represents the rotation angle of the DP with respect to a fixed reference axis. The total effect of the DP on the OAM-carrying beam can be compactly expressed through the following Jones matrix:

$$T = \begin{bmatrix} e^{-2il(\varphi+\phi)} & 0 \\ 0 & e^{2il(\varphi+\phi)} \end{bmatrix}. \tag{4.18}$$

4.3 Jones matrix representation for vector beams

As it was mentioned in the last sections, the effect of the DP can be represented by Jones matrices which depend on the Fresnel coefficients and the rotation angle of the

prism. In addition to these matrices, we propose an extra matrix that represents the OAM inversion. Since this inversion is due to internal total reflection in the prism, the reflection matrix defined in eq. 4.14, and the inversion matrix defined in eq. 4.18 must be merged, resulting in the following matrix

$$L = \frac{1}{2}\begin{bmatrix} e^{-2il(\varphi+\phi)}\left(r_{2\parallel}+r_{2\perp}\right) & r_{2\parallel}-r_{2\perp} \\ r_{2\parallel}-r_{2\perp} & e^{2il(\varphi+\phi)}\left(r_{2\parallel}+r_{2\perp}\right) \end{bmatrix}. \tag{4.19}$$

Therefore, the incoming electric field $\mathbf{E_0}$ will be transformed by the prism as follows:

$$\mathbf{E} = R'\, t'_3\, L\, t'_1\, \mathbf{E_0}. \tag{4.20}$$

4.4 Numerical Simulation

In this section, we describe the numerical implementation used to analyze the effect of a DP on vector beams. The simulation considers a beam of wavelength $\lambda = 633$ nm and an initial waist proportional to $\rho_0 = 1.5$ mm. The DP is characterized by a refractive index $n = 1.51509$ and an inclination angle of its first interface set at $45°$. The incident beam is generated using a q-plate function, which decomposes it into right- and left-handed circular polarization components:

$$E_R = \cos(\Theta)u_1, \tag{4.21}$$

$$E_L = e^{i\delta}\sin(\Theta)u_2, \tag{4.22}$$

where u_1 and u_2 represent the spatial field distributions for different OAM values, and like in eq. (2.8) Θ represent the weight of the superposition. The transformation induced by the prism is described using a Jones matrix formalism, which combines the effects (OAM and polarization) of the three interfaces within the prism. The total transformation matrix T is computed at each point (i, j) of the grid using the relation:

$$T_{(i,j)} = R_{(i,j)}t_{3(i,j)}L_{(i,j)}t_{1(i,j)}, \tag{4.23}$$

The transformed polarization components are computed as:

$$E'_R = T_{11}E_R + T_{12}E_L, \tag{4.24}$$

$$E'_L = T_{21}E_R + T_{22}E_L. \tag{4.25}$$

From these, the final polarization states (horizontal, vertical, diagonal, and circular) are reconstructed, and the Stokes parameters are obtained. The simulation results are visualized through Stokes parameter mappings and intensity distributions, which provide insights into the beam's polarization transformation induced by the DP as observed in *Figure 4.5*.

4.5 Experiment set up

The experimental arrangement used to study the effect of the DP on vector beams is shown in Figure 4.6. The system begins with a linearly polarized laser, which serves as the light source. To control the polarization state, the beam first passes through a half-wave plate (HWP 1), which adjusts it to either horizontal or vertical polarization. The beam then impinges on a q-plate, generating a vector beam. A second half-wave plate (HWP 2) placed after the q-plate converts right-handed circular polarization into left-handed circular polarization, enabling the generation of hybrid vector modes. The resulting beam enters the DP, which is rotated at controlled angles to induce transformations in the beam's polarization distribution.

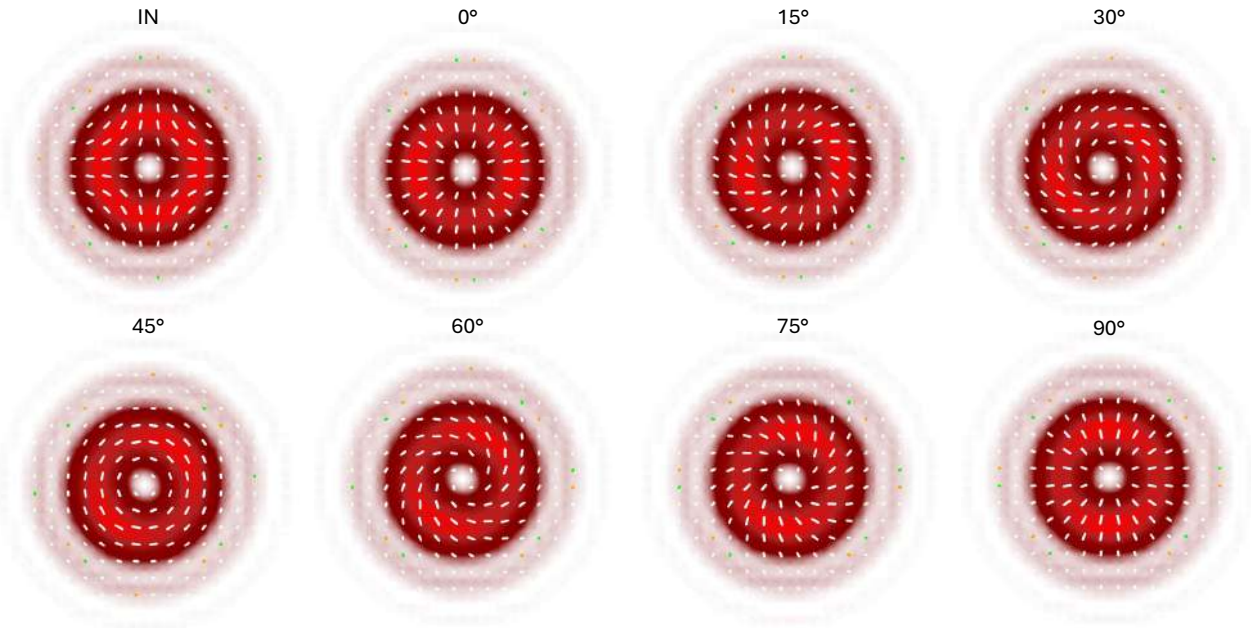

Figure 4.5: Polarization distribution of the vector beam after interaction with the DP. The image labeled as "IN" corresponds to the input beam, while the remaining images show the resulting beams for prism rotations from 0° to 90° in 15° increments. The OAM value inversion caused by the reflection inside the DP is observed, along with a smooth transition from a radially polarized beam to an azimuthally polarized one.

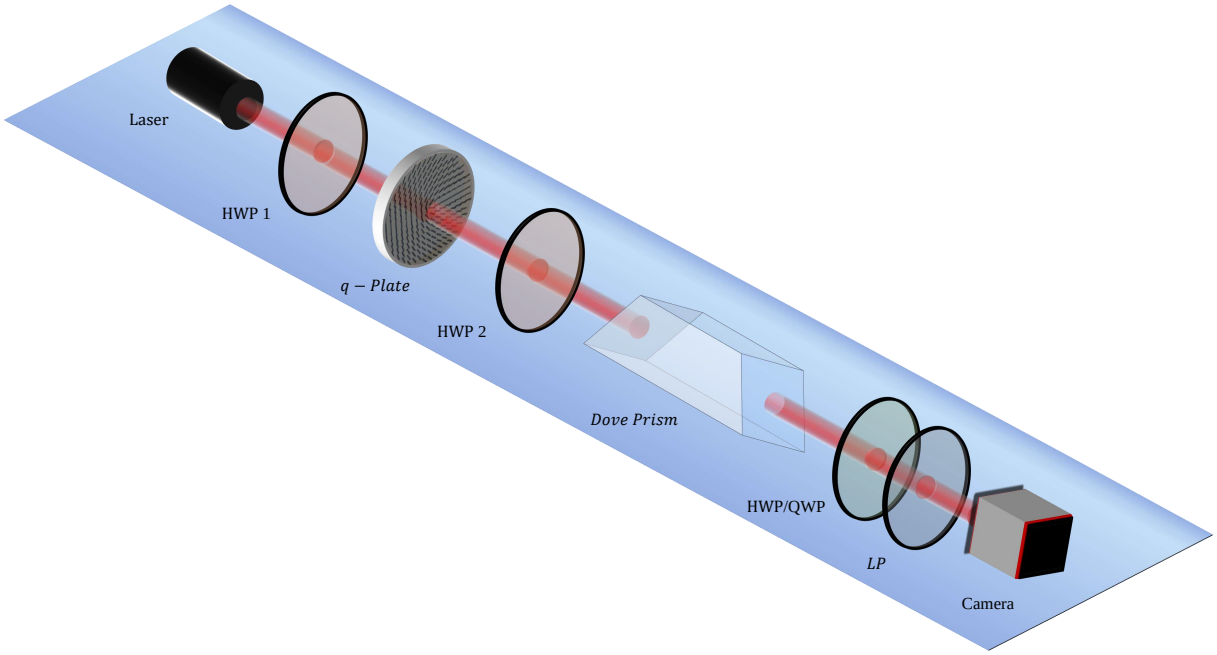

Figure 4.6: Experimental setup used to study the effect of the DP on vector beams. A linearly polarized laser generates the initial beam, which is later modified by a q-plate to produce a vector beam. A DP is introduced and rotated, and the output beam is analyzed using Stokes polarimetry.

To analyze the beam after its interaction with the DP, a Stokes polarimetry setup is placed at the output. Before introducing the prism, Stokes measurements are performed to characterize the input beam, labeled as *IN* in Figure 4.7. Once the initial characterization is complete, the DP is introduced and rotated in 15° increments from 0° to 90°. After each rotation, Stokes parameters are measured again to monitor the evolution of the beam's polarization and phase structure.

4.6 Experimental results

Figure 4.7 presents the polarization distributions obtained from the experimental setup. When the DP was set at 0°, the output beam exhibited a clear radial polarization pattern, consistent with theoretical predictions. This behavior confirms the expected inversion of the OAM charge induced by the prism. As the DP rotation angle increased, the output beam displayed a continuous transformation in its polarization state. In addition to inverting the OAM charge, the prism introduced an intermodal phase difference that led to the formation of spiral polarization patterns. At 45°, the beam showed azimuthal polarization, and further rotations produced additional spiral configurations. Notably, at 90°, the radial polarization state reappeared, indicating the completion of a full po-

larization transformation cycle. Since this behavior is periodic with respect to ϕ, the experimental and simulation measurements were limited to the interval between 0° and 90°.

The experimental results shown in Figure 4.7 are in excellent agreement with the simulated results presented in Figure 4.5. Minor discrepancies, such as the presence of elliptical polarization states in a few cases, are attributed to slight misalignments of the DP during the experiment.

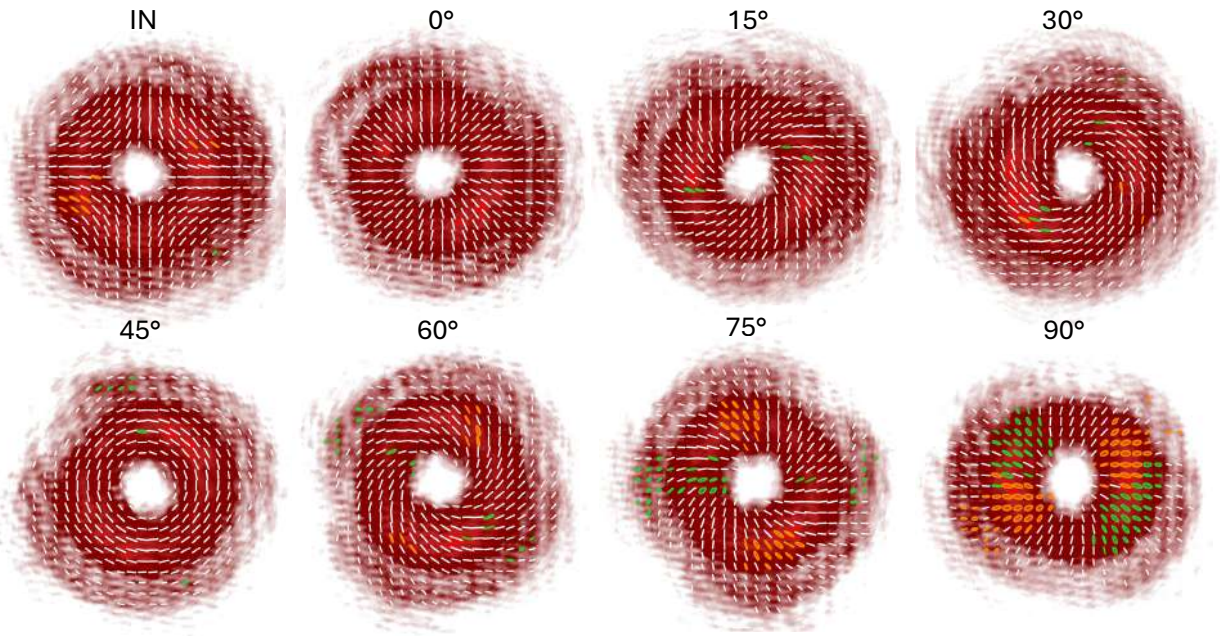

Figure 4.7: Experimental results showing the polarization distribution of an optical vortex beam passing through a DP. The beam labeled *IN* corresponds to the incident beam, while the remaining beams represent the output after propagation through the prism. Measurements were taken at rotation angles from 0° to 90° in 15° increments. White lines indicate the polarization orientation, with intensity distribution shown in red. Green regions highlight variations due to experimental imperfections.

5 | Conclusions and further work

Vectorial structured light beams are recognized for the coupling of two of their DoFs: polarization and OAM. These beams have gained popularity in recent years due to their unique properties, motivating the exploration of novel methods for their generation and the development of new beam types. The present work discusses two novel forms of vector beams, the Pearcey-Gauss and the curvilinear, which have been constructed for the first time.

The primary objective of this thesis is to analyze the effect of the DP on vortex vector beams. This intention arises from earlier investigations that established that the prism has a strong impact on polarization and OAM independently; however, no research has examined the scenario in which one cannot be modified without affecting the other, as is observed with vector beams. This investigation shows that the effect of the DP on vector beams differs from what was expected due to the coupling between the beam's polarization and OAM. Estimating the effect on vector beams by just considering polarization suggests that a linearly polarized pattern would evolve into a pattern exhibiting both linear and elliptical polarizations, depending on its orientation with respect to the prism. In contrast, paying attention just to the OAM effect would suggest that the OAM value would reverse and the beam would rotate similarly to a picture as the prism rotates. Nevertheless, the results of this study provide a different behavior, established by calculations, simulations, and validated by experiments. As a result, a Jones matrix representing the prism's total effect on both OAM and polarization was formulated, and programs were created to simulate this phenomenon. The empirical results found agree well with these models, offering solid validation for the theoretical predictions. A key finding is that when polarization and OAM are coupled as a vector beam, the DP not only reverses the sign of the OAM but also produces an intermodal phase shift. It led to a smooth transition between fundamental vector beam types, namely azimuthal and radial polarizations, in conjunction with their hybrid states.

Bibliography

[1] A. Forbes, A. Dudley, and M. McLaren, "Creation and detection of optical modes with spatial light modulators," *Adv. Opt. Photon.*, vol. 8, no. 2, pp. 200–227, Jun 2016. [Online]. Available: https://opg.optica.org/aop/abstract.cfm?URI=aop-8-2-200

[2] C. Rosales-Guzmán and A. Forbes, *How to Shape Light with Spatial Light Modulators*. SPIE Press, 1 2017. [Online]. Available: https://doi.org/10.1117/3.2281295

[3] M. Padgett and R. Bowman, "Tweezers with a twist," *Nature photonics*, vol. 5, no. 6, pp. 343–348, 2011.

[4] B. Jack, J. Leach, H. Ritsch, S. Barnett, M. Padgett, and S. Franke-Arnold, "Precise quantum tomography of photon pairs with entangled orbital angular momentum," *New Journal of Physics*, vol. 11, no. 10, p. 103024, 2009.

[5] A. E. Willner, H. Huang, Y. Yan, Y. Ren, N. Ahmed, G. Xie, C. Bao, L. Li, Y. Cao, Z. Zhao *et al.*, "Optical communications using orbital angular momentum beams," *Advances in optics and photonics*, vol. 7, no. 1, pp. 66–106, 2015.

[6] C. Maurer, A. Jesacher, S. Bernet, and M. Ritsch-Marte, "What spatial light modulators can do for optical microscopy," *Laser & Photonics Reviews*, vol. 5, no. 1, pp. 81–101, 2011.

[7] G. Nehmetallah and P. P. Banerjee, "Applications of digital and analog holography in three-dimensional imaging," *Advances in Optics and Photonics*, vol. 4, no. 4, pp. 472–553, 2012.

[8] W. Osten, A. Faridian, P. Gao, K. Körner, D. Naik, G. Pedrini, A. K. Singh, M. Takeda, and M. Wilke, "Recent advances in digital holography," *Applied optics*, vol. 53, no. 27, pp. G44–G63, 2014.

[9] P. Memmolo, L. Miccio, M. Paturzo, G. D. Caprio, G. Coppola, P. A. Netti, and P. Ferraro, "Recent advances in holographic 3d particle tracking," *Advances in Optics and Photonics*, vol. 7, no. 4, pp. 713–755, 2015.

[10] L. Burger, I. Litvin, S. Ngcobo, and A. Forbes, "Implementation of a spatial light modulator for intracavity beam shaping," *Journal of Optics*, vol. 17, no. 1, p. 015604, 2014.

[11] S. Ngcobo, I. Litvin, L. Burger, and A. Forbes, "A digital laser for on-demand laser modes," *Nature communications*, vol. 4, no. 1, p. 2289, 2013.

[12] J. W. Goodman, *Introduction to Fourier optics*. Roberts and Company publishers, 2005.

[13] A. E. Siegman, *Lasers*. University science books, 1986.

[14] R. Jáuregui and S. Hacyan, "Quantum-mechanical properties of bessel beams," *Physical Review A—Atomic, Molecular, and Optical Physics*, vol. 71, no. 3, p. 033411, 2005.

[15] A. Dudley, Y. Li, T. Mhlanga, M. Escuti, and A. Forbes, "Generating and measuring nondiffracting vector bessel beams," *Optics letters*, vol. 38, no. 17, pp. 3429–3432, 2013.

[16] E. J. Galvez, S. Khadka, W. H. Schubert, and S. Nomoto, "Poincaré-beam patterns produced by nonseparable superpositions of laguerre-gauss and polarization modes of light," *Applied optics*, vol. 51, no. 15, pp. 2925–2934, 2012.

[17] B. Rodríguez-Lara and R. Jáuregui, "Dynamical constants for electromagnetic fields with elliptic-cylindrical symmetry," *Physical Review A—Atomic, Molecular, and Optical Physics*, vol. 78, no. 3, p. 033813, 2008.

[18] C. Rosales-Guzmán, X.-B. Hu, V. Rodríguez-Fajardo, R. I. Hernandez-Aranda, A. Forbes, and B. Perez-Garcia, "Experimental generation of helical mathieu–gauss vector modes," *Journal of Optics*, vol. 23, no. 3, p. 034004, 2021.

[19] Y.-L. Yao-Li, X.-B. Hu, B. Perez-Garcia, B.-Z. Bo-Zhao, W. Gao, Z.-H. Zhu, and C. Rosales-Guzmán, "Classically entangled ince–gaussian modes," *Applied Physics Letters*, vol. 116, no. 22, 2020.

[20] B. Rodríguez-Lara and R. Jáuregui, "Dynamical constants of structured photons with parabolic-cylindrical symmetry," *Physical Review A—Atomic, Molecular, and Optical Physics*, vol. 79, no. 5, p. 055806, 2009.

[21] B. Zhao, V. Rodríguez-Fajardo, X.-B. Hu, R. I. Hernandez-Aranda, B. Perez-Garcia, and C. Rosales-Guzmán, "Parabolic-accelerating vector waves," *Nanophotonics*, vol. 11, no. 4, pp. 681–688, 2022.

[22] E. Medina-Segura, L. Miranda-Culin, V. Rodríguez-Fajardo, B. Perez-Garcia, and C. Rosales-Guzmán, "Helico-conical vector beams," *Optics Letters*, vol. 48, no. 18, pp. 4897–4900, 2023.

[23] V. Rodríguez-Fajardo, G. Flores-Cova, C. Rosales-Guzmán, and B. Perez-Garcia, "Experimental generation of scalar and vector vortex pearcey–gauss beams," *Journal of Physics: Photonics*, vol. 6, no. 4, p. 045015, 2024.

[24] B. E. Saleh and M. C. Teich, *Fundamentals of photonics*. john Wiley & sons, 2019.

[25] K. Floettmann, "Coherent superposition of orthogonal hermite–gauss modes," *Optics Communications*, vol. 505, p. 127537, 2022. [Online]. Available: https://www.sciencedirect.com/science/article/pii/S0030401821007860

[26] Y. Yang, Y. Li, and C. Wang, "Generation and expansion of laguerre–gaussian beams," *Journal of Optics*, vol. 51, no. 4, pp. 910–926, 2022.

[27] J. P. C. Narag and N. Hermosa, "Probing higher orbital angular momentum of laguerre-gaussian beams via diffraction through a translated single slit," *Physical Review Applied*, vol. 11, no. 5, p. 054025, 2019.

[28] Y. Shen and C. Rosales-Guzmán, "Nonseparable states of light: From quantum to classical," *Laser & Photonics Reviews*, vol. 16, no. 7, p. 2100533, 2022. [Online]. Available: https://onlinelibrary.wiley.com/doi/abs/10.1002/lpor.202100533

[29] Q. Zhan, "Cylindrical vector beams: from mathematical concepts to applications," *Advances in Optics and Photonics*, vol. 1, no. 1, pp. 1–57, 2009.

[30] A. Rubano, F. Cardano, B. Piccirillo, and L. Marrucci, "Q-plate technology: a progress review," *JOSA B*, vol. 36, no. 5, pp. D70–D87, 2019.

[31] W. Shu, X. Ling, X. Fu, Y. Liu, Y. Ke, and H. Luo, "Polarization evolution of vector beams generated by q-plates," *Photonics Research*, vol. 5, no. 2, pp. 64–72, 2017.

[32] L. Marrucci, C. Manzo, and D. Paparo, "Optical spin-to-orbital angular momentum conversion in inhomogeneous anisotropic media," *Phys. Rev. Lett.*, vol. 96, p. 163905, Apr 2006. [Online]. Available: https://link.aps.org/doi/10.1103/PhysRevLett.96.163905

[33] L. Marrucci, “The q-plate and its future,” *Journal of Nanophotonics*, vol. 7, no. 1, pp. 078 598–078 598, 2013.

[34] V. Arrizón, U. Ruiz, R. Carrada, and L. A. González, “Pixelated phase computer holograms for the accurate encoding of scalar complex fields,” *Journal of the Optical Society of America A*, vol. 24, no. 11, pp. 3500–3507, 2007.

[35] B. Perez-Garcia, C. López-Mariscal, R. I. Hernandez-Aranda, and J. C. Gutiérrez-Vega, “On-demand tailored vector beams,” *Applied Optics*, vol. 56, no. 24, pp. 6967–6972, 2017.

[36] D. H. Goldstein, *Polarized light*. CRC Press, 2011.

[37] E. Collett, “Polarized light. fundamentals and applications,” *Optical Engineering*, 1992.

[38] C. Huygens, *Traité de la lvmière: où sont expliquées les causes de ce qui luy arrive dans la réflexion & dans la réfraction, et particulièrement dans l’étrange réfraction dv cristal d’Islande*. Pierre vander Aa, 1967.

[39] T. Pearcey, “Xxxi. the structure of an electromagnetic field in the neighbourhood of a cusp of a caustic,” *The London, Edinburgh, and Dublin Philosophical Magazine and Journal of Science*, vol. 37, pp. 311–317, 1946.

[40] J. D. Ring, J. Lindberg, A. Mourka, M. Mazilu, K. Dholakia, and M. R. Dennis, “Auto-focusing and self-healing of pearcey beams,” *Opt. Express*, vol. 20, no. 17, pp. 18 955–18 966, Aug 2012.

[41] Y. Liu, C. Xu, Z. Lin, Y. Wu, Y. Wu, L. Wu, and D. Deng, “Auto-focusing and self-healing of symmetric odd-pearcey gauss beams,” *Optics Letters*, vol. 45, no. 11, pp. 2957–2960, 2020.

[42] K. Cheng, G. Lu, and X. Zhong, “Energy flux density and angular momentum density of pearcey-gauss vortex beams in the far field,” *Applied Physics B*, vol. 123, no. 2, p. 60, 2017.

[43] J. Wu, C. Xu, L. Wu, and D. Deng, “Propagation dynamics of the pearcey gaussian vortex beams in a harmonic potential,” *Optics Communications*, vol. 478, p. 126367, 1 2021.

[44] X. W. Sun, Y. J. Liu, D. Luo, and H. T. Dai, “Propagation dynamics of an optical vortex imposed on an airy beam,” *Optics Letters, Vol. 35, Issue 23, pp. 4075-4077*, vol. 35, pp. 4075–4077, 12 2010.

[45] ——, “Propagation properties of an optical vortex carried by an airy beam: experimental implementation,” *Optics Letters, Vol. 36, Issue 9, pp. 1617-1619*, vol. 36, pp. 1617–1619, 5 2011.

[46] E. Otte, C. Alpmann, and C. Denz, “Higher-order polarization singularities in tailored vector beams,” *J. Opt.*, vol. 18, p. 074012, 2016.

[47] J. W. Goodman, *Introduction to Fourier Optics*, 4th ed. New York: W. H. Freeman, 2017.

[48] C. Rosales-Guzmán and A. Forbes, *Structured Light with Spatial Light Modulators*, 2nd ed. Bellingham: SPIE, 2024.

[49] M. S. Scholl, “Ray trace through a corner-cube retroreflector with complex reflection coefficients,” *JOSA A*, vol. 12, no. 7, pp. 1589–1592, 1995.

[50] S. Qian, W. Jark, G. Sostero, A. Gambitta, F. Mazzolini, and A. Savoia, “Precise measuring method for detecting the in situ distortion profile of a high-heat-load mirror for synchrotron radiation by use of a pentaprism long trace profiler,” *Applied Optics*, vol. 36, no. 16, pp. 3769–3775, 1997.

[51] J. Feng, X. Fang, X. Cao, C. Ma, Q. Dai, H. Zhu, and Y. Wang, “Advanced hyperspectral video imaging system using amici prism,” *Optics express*, vol. 22, no. 16, pp. 19 348–19 356, 2014.

[52] M. S. Rao, “Methods for making prisms with submultiple or half angles: applications to the measurement of the angles of pechan and pellin-broca prisms,” *Optical Engineering*, vol. 41, no. 11, pp. 2945–2950, 2002.

[53] R. Gonzalez-Romero, M. Strojnik, and G. Garcia-Torales, “Theory of a rotationally shearing interferometer,” *Journal of the Optical Society of America A*, vol. 38, no. 2, pp. 264–270, Feb 2021. [Online]. Available: http://opg.optica.org/josaa/abstract.cfm?URI=josaa-38-2-264

[54] W. L. Wolfe, “Nondispersive prisms,” *The Handbook of Optics*, vol. 2, pp. 4–1, 1995.

[55] E. Hecht and A. Zajac, *Óptica*. Pearson, 1980.

[56] D. Malacara, *Óptica básica*. Fondo de cultura económica, 2015.

[57] N. González, G. Molina-Terriza, and J. P. Torres, “How a dove prism transforms the orbital angular momentum of a light beam,” *Optics express*, vol. 14, no. 20, pp. 9093–9102, 2006.

[58] C. Gao, X. Qi, Y. Liu, J. Xin, and L. Wang, “Sorting and detecting orbital angular momentum states by using a dove prism embedded mach–zehnder interferometer and amplitude gratings,” *Optics Communications*, vol. 284, no. 1, pp. 48–51, 2011. [Online]. Available: https://www.sciencedirect.com/science/article/pii/S0030401810009466

[59] S. Karan, Ruchi, P. Mohta, and A. K. Jha, “Quantifying polarization changes induced by rotating dove prisms and k-mirrors,” *Applied Optics*, vol. 61, no. 28, pp. 8302–8307, 2022.

[60] Y. Yao, X. Liang, M. Zhu, W. Zhu, J. Geng, and R. Jin, “Analysis and experiments on reflection and refraction of orbital angular momentum waves,” *IEEE Transactions on Antennas and Propagation*, vol. 67, no. 4, pp. 2085–2094, 2019.

[61] D. L. Andrews and K. A. Forbes, “Quantum features in the orthogonality of optical modes for structured and plane-wave light,” *Optics Letters*, vol. 43, no. 14, pp. 3249–3252, 2018.

[62] M. Padgett and L. Allen, “Light with a twist in its tail,” *Contemporary physics*, vol. 41, no. 5, pp. 275–285, 2000.